

REPORT DOCUMENTATION PAGE

Form Approved
OMB No. 0704-0188

Public reporting burden for this collection of information is estimated to average 1 hour per response, including the time for reviewing instructions, searching existing data sources, gathering and maintaining the data needed, and completing and reviewing this collection of information. Send comments regarding this burden estimate or any other aspect of this collection of information, including suggestions for reducing this burden to Department of Defense, Washington Headquarters Services, Directorate for Information Operations and Reports (0704-0188), 1215 Jefferson Davis Highway, Suite 1204, Arlington, VA 22202-4302. Respondents should be aware that notwithstanding any other provision of law, no person shall be subject to any penalty for failing to comply with a collection of information if it does not display a currently valid OMB control number. **PLEASE DO NOT RETURN YOUR FORM TO THE ABOVE ADDRESS.**

1. REPORT DATE (DD-MM-YYYY) 17-07-2007		2. REPORT TYPE Journal Article		3. DATES COVERED (From - To)	
4. TITLE AND SUBTITLE Dynamics of Hyperthermal Collisions of O(³P) with CO (Preprint)				5a. CONTRACT NUMBER F04611-03-C-0015	
				5b. GRANT NUMBER	
				5c. PROGRAM ELEMENT NUMBER	
6. AUTHOR(S) A. Brunsvold, H. Upadhyaya, J. Zhang, R. Cooper, T. Minton (Montana State Univ.); M. Braunstein, J. Duff (Spectral Sciences, Inc.)				5d. PROJECT NUMBER	
				5e. TASK NUMBER BMSBR2FT	
				5f. WORK UNIT NUMBER	
7. PERFORMING ORGANIZATION NAME(S) AND ADDRESS(ES) Spectral Sciences Incorporated 4 Fourth Avenue Burlington MA 01803-3304				8. PERFORMING ORGANIZATION REPORT NUMBER AFRL-PR-ED-JA-2007-358	
9. SPONSORING / MONITORING AGENCY NAME(S) AND ADDRESS(ES) Air Force Research Laboratory (AFMC) AFRL/PRS 5 Pollux Drive Edwards AFB CA 93524-7048				10. SPONSOR/MONITOR'S ACRONYM(S)	
				11. SPONSOR/MONITOR'S NUMBER(S) AFRL-PR-ED-JA-2007-358	
12. DISTRIBUTION / AVAILABILITY STATEMENT Approved for public release; distribution unlimited (PA #07292A).					
13. SUPPLEMENTARY NOTES Submitted for publication in the Journal of Physical Chemistry					
14. ABSTRACT The dynamics of O(3P) + CO collisions at a hyperthermal collision energy of 83 kcal mol ⁻¹ have been studied with a crossed molecular beams experiment and with quasiclassical trajectory calculations on computed potential energy surfaces. In the experiment, a rotatable mass spectrometer detector was used to monitor inelastically and reactively scattered products as a function of velocity and scattering angle. From these data, center-of-mass (c.m.) translational energy and angular distributions were derived for the inelastic and reactive channels. Isotopically labeled C18O was used to distinguish the reactive channel (16O + C18O → 16OC + 18O) from the inelastic channel (16O + C18O → 16O + C18O). The reactive 16OC molecules scattered predominantly in the forward direction—i.e., in the same direction as the velocity vector of the reagent O atoms in the c.m. frame. The c.m. translational energy distribution of the reactively scattered 16OC and 18O was very broad, indicating that 16OC is formed with a wide range of internal energies, with an average internal excitation of 60 percent of the available energy. The c.m. translational energy distribution of the inelastically scattered C18O and 16O products indicated that an average of 15 percent of the collision energy went into internal excitation of C18O, although a small fraction of the collisions transferred nearly all the collision energy into internal excitation of C18O. The theoretical calculations, which extend previously published results on this system, predict c.m. translational and angular distributions that are in near quantitative agreement with the experimentally derived distributions. The theoretical calculations, thus validated by the experimental results, have been used to derive internal state distributions of scattered CO products and to probe in detail the interactions that lead to the observed dynamical behavior.					
15. SUBJECT TERMS					
16. SECURITY CLASSIFICATION OF:			17. LIMITATION OF ABSTRACT	18. NUMBER OF PAGES	19a. NAME OF RESPONSIBLE PERSON
a. REPORT	b. ABSTRACT	c. THIS PAGE			19b. TELEPHONE NUMBER <i>(include area code)</i>
Unclassified	Unclassified	Unclassified	SAR	59	N/A

Dynamics of Hyperthermal Collisions of O(³P) with CO (Preprint)

Amy L. Brunsvold, Hari P. Upadhyaya, Jianming Zhang, Russell Cooper,
and Timothy K. Minton*

Department of Chemistry and Biochemistry

Montana State University

Bozeman, Montana 59717

Email: tminton@montana.edu

Matthew Braunstein* and James W. Duff

Spectral Sciences, Incorporated

Burlington, MA 01803

ABSTRACT

The dynamics of O(³P) + CO collisions at a hyperthermal collision energy of 83 kcal mol⁻¹ have been studied with a crossed molecular beams experiment and with quasiclassical trajectory calculations on computed potential energy surfaces. In the experiment, a rotatable mass spectrometer detector was used to monitor inelastically and reactively scattered products as a function of velocity and scattering angle. From these data, center-of-mass (c.m.) translational energy and angular distributions were derived for the inelastic and reactive channels. Isotopically labeled C¹⁸O was used to distinguish the reactive channel (¹⁶O + C¹⁸O → ¹⁶OC + ¹⁸O) from the inelastic channel (¹⁶O + C¹⁸O → ¹⁶O + C¹⁸O). The reactive ¹⁶OC molecules scattered predominantly in the forward direction—i.e., in the same direction as the velocity vector of the reagent O atoms in the c.m. frame. The c.m. translational energy distribution of the

reactively scattered ^{16}OC and ^{18}O was very broad, indicating that ^{16}OC is formed with a wide range of internal energies, with an average internal excitation of 60 percent of the available energy. The c.m. translational energy distribution of the inelastically scattered C^{18}O and ^{16}O products indicated that an average of 15 percent of the collision energy went into internal excitation of C^{18}O , although a small fraction of the collisions transferred nearly all the collision energy into internal excitation of C^{18}O . The theoretical calculations, which extend previously published results on this system, predict c.m. translational and angular distributions that are in near quantitative agreement with the experimentally derived distributions. The theoretical calculations, thus validated by the experimental results, have been used to derive internal state distributions of scattered CO products and to probe in detail the interactions that lead to the observed dynamical behavior.

I. INTRODUCTION

Hyperthermal oxygen-atom collisions are abundant on and around space vehicles that travel at high velocities through the rarefied atmosphere of the Earth at altitudes of 150-700 km. In this region of the upper atmosphere, atomic oxygen (and, with a lower flux, molecular nitrogen) can collide with space vehicles and their exhaust streams at relative velocities in the vicinity of 8 km s^{-1} .¹⁻⁴ These high relative velocities may lead to gas-phase collisions with more than $100 \text{ kcal mol}^{-1}$ of collision energy in the center-of-mass (c.m.) reference frame.⁴ Such collisions may result in large energy transfers into product internal degrees of freedom and the opening of reaction channels with high barriers.

Hyperthermal collisions between $O(^3P)$ and the common combustion product, $CO(^1\Sigma^+)$, have received a great deal of attention. When the reactants and products are in their electronic ground states, the possible outcomes of such collisions are:



At a typical relative velocity of 8 km s^{-1} , the c.m. collision energy of $O + CO$ is $77.9 \text{ kcal mol}^{-1}$. If exhaust gases were directed at 3 km s^{-1} into the ram direction of a spacecraft, the relative velocity of O and CO could be $\sim 11 \text{ km s}^{-1}$, in which case the c.m. collision energy would be $147 \text{ kcal mol}^{-1}$. Achieving the collision energy needed for the formation of molecular oxygen (3) would require relative velocities that are unattainable under any reasonable operating conditions. Therefore, the only channels that are accessible at the collision energies relevant to exhaust gases from space vehicles in the upper atmosphere are (1) and (2). Upschulte and Caledonia⁵ measured infrared emission of vibrationally excited CO following collisions between atomic oxygen and CO at relative velocities of approximately 8 km s^{-1} , and they reported a cross section for vibrational excitation, $\sum_{i=1} i\sigma(v=i)$, for $CO(v)$ of $7.3 \times 10^{-17} \text{ cm}^2$. From their measured spectra, they concluded that the CO molecules were highly vibrationally excited, up to $CO(v=11)$. Their result presumably contained contributions from both inelastic and reactive scattering. A space-based study by Green and coworkers,⁶ where optical emission spectra were measured from a remote spacecraft after CO gas was released from a canister in low Earth orbit, determined that bright infrared emissions in both fundamental and overtone vibrational bands

resulted from the highly energetic interaction of the released CO with ambient O(3P) at relative velocities of $\sim 8 \text{ km s}^{-1}$. Their measured spectra showed substantial rotational and vibrational excitation in the CO product, closely matching the results of Upschulte and Caledonia. Green *et al.*⁶ estimated the cross section to create vibrationally excited CO(v) to be on the order of 10^{-16} cm^2 , in reasonable agreement with the results of Upschulte and Caledonia.

Braunstein and Duff⁷ computed the potential energy surfaces of the three lowest electronic triplet states of CO₂ (one $^3A'$ state and two $^3A''$ states), which correlate with O(3P) + CO($^1\Sigma^+$). In addition, they ran classical trajectories on these surfaces. Fig. 1 shows the calculated potential energy curves of the ground singlet state of CO₂($^1A'$) and the three lowest triplet states, with the O–C–O angle equal to 120° . The energy shown here is a function of one of the CO bond lengths, while the length of the other CO bond is fixed at 1.2 \AA . For the lowest triplet state at its transition state geometry, which is slightly different than shown in the figure, the barrier to O-atom exchange, Eq. (2), was calculated to be $4.6 \text{ kcal mol}^{-1}$. Although coupling to the singlet ground state is spin-forbidden from the three lowest-lying triplet states, the singlet potential energy surface (the ground state of CO₂, X $^1\Sigma_g^+$) crosses the triplet surface and leads to a higher dissociation limit, with products, O(1D) + CO($^1\Sigma^+$), about 46 kcal mol^{-1} above the dissociation limit that leads to O(3P) + CO($^1\Sigma^+$). Intersystem crossing (ISC) is thus possible, although spin conservation is generally favored for systems containing first-row atoms, and other studies involving hyperthermal O-atom reactions showed no evidence for ISC.^{8,9} Quasiclassical trajectory calculations on the computed triplet surfaces⁷ agreed well with available kinetic data on vibrational relaxation of CO($v=1 \rightarrow v=0$) by O(3P), except at low temperature. The shape of the emission spectra of CO based on the calculations for collisions at a relative velocity of 8 km s^{-1} were in fair agreement with the experimental observations of Upschulte and Caledonia and

with the spaced-based observations of Green *et al.* However, the magnitude of the calculated cross section for the formation of vibrationally excited CO was about an order of magnitude above the two experimental values. A subsequent modeling study¹⁰ suggested that the difference in cross sections between the measured Upschulte and Caledonia result and the calculations of Braunstein and Duff was the result of multiple-collision effects not fully accounted for in the measurements, although this suggestion has not been experimentally confirmed. The calculated trajectories were studied to learn mechanistic details of the collisions that lead to vibrational excitation through inelastic and reactive collisions. It was found that these processes occur when the reagent O atom approaches the carbon end of CO on the two low-lying triplet surfaces, $^3A'$ and $1^3A''$, which have small wells, at O–C–O angles between 80° and 140°.

We describe here a combined theoretical and crossed-molecular-beams study of $O(^3P) + CO$ collisions at a hyperthermal collision energy near 80 kcal mol⁻¹ ($E_{\text{coll}} = 79.9$ kcal mol⁻¹ for the theoretical calculations and $\langle E_{\text{coll}} \rangle = 83$ kcal mol⁻¹ for the experiment). Isotopic substitution was used in the experiment to distinguish between the reactive channel, $^{16}\text{O} + \text{C}^{18}\text{O} \rightarrow ^{16}\text{OC} + ^{18}\text{O}$, Eq. (2), and the inelastic channel, $^{16}\text{O} + \text{C}^{18}\text{O} \rightarrow ^{16}\text{O} + \text{C}^{18}\text{O}$, Eq. (1). We investigated the dynamics of the reactive and inelastic pathways, including the disposal of energy in the products and the angular distributions of the scattered products. Using the surfaces of Ref. 7, new quasiclassical trajectory (QCT) calculations were performed which extend previous results to facilitate direct comparisons with the present measurements and to more fully explore the dynamics. The results of the QCT calculations are in almost quantitative agreement with the present experimental data.

II. THEORETICAL DETAILS

A. Methods. The theoretical methods are based on the potential surfaces and quasi-classical trajectory (QCT) procedures of Braunstein and Duff.⁷ We use the same surfaces of Braunstein and Duff, and we extend the QCT calculations to generate new cross section results that can be compared directly with the experimental data discussed in this paper and at several collision energies well below and above those used in the experiment. The present work provides new and extensive results that separate the reactive and inelastic cross sections. The present results also use at least an order of magnitude more trajectories per collision energy than the earlier work for improved statistical convergence.

Potential energy surfaces. We briefly review the key features of the potential energy surfaces used. Complete details can be found elsewhere.⁷ Figure 1 shows the basic features of the relevant potentials. Collisions of $O(^3P)$ with $CO(^1\Sigma^+)$ correlate to three electronic states of CO_2 , all triplets: a single $^3A'$ state and two $^3A''$ states. The five nearby singlet states, which can only participate through weak spin-orbit interactions, lead to $O(^1D)$ and $CO(^1\Sigma^+)$, about 46 kcal mol⁻¹ above the $O(^3P) + CO(^1\Sigma^+)$ threshold. One of these five singlet states leads to the $^1\Sigma_g^+$ ground state of CO_2 about 127 kcal mol⁻¹ below the $O(^3P) + CO(^1\Sigma^+)$ threshold. The remainder are relatively high in energy and give rise to some of the complex features in the CO_2 UV photoabsorption spectrum starting about 23 kcal mol⁻¹ above the $O(^3P) + CO(^1\Sigma^+)$ threshold.¹¹ As in our earlier work,⁷ we ignore spin-orbit interactions that could mix the singlet and triplet states.

The potentials used are global fits of ~320 separate *ab initio* calculations of the three lowest triplet states of CO_2 . The *ab initio* calculations were performed at the (12 electron, 10 orbital) CASSCF-MP2 level, within a modest 631+G(d) basis set, with the electronic structure

code, GAMESS.¹² The lowest two states, $^3A'$ and $1^3A''$, have well depths of $21.7 \text{ kcal mol}^{-1}$ and $25.1 \text{ kcal mol}^{-1}$, respectively. These minima occur near the geometries shown in Figure 1. For the $^3A'$ state the minimum occurs at $r_1=r_2=1.26 \text{ \AA}$, $\theta = 118^\circ$, and for the $1^3A''$ state the minimum occurs at $r_1=r_2=1.27 \text{ \AA}$, $\theta = 127^\circ$. The $2^3A''$ state is mostly repulsive and has a saddle point with C_{2v} geometry. The $^3A'$ and $1^3A''$ states have small barriers of $4.6 \text{ kcal mol}^{-1}$ and $6.9 \text{ kcal mol}^{-1}$, respectively, which occur at Cs geometries of their transition states near to those shown in Figure 1. These transition states are in bent C_s geometries, where for the $^3A'$ state, $r_1 = 1.16 \text{ \AA}$, $r_2 = 2.0 \text{ \AA}$, $\theta = 112^\circ$, and for the $1^3A''$ state, $r_1 = 1.16 \text{ \AA}$, $r_2 = 1.85 \text{ \AA}$, $\theta = 122^\circ$. The *ab initio* points of the three electronic states were globally fit with the method of Aguado and Paniagua.¹³

Dynamics and cross sections. The three lowest triplet potential energy surfaces were used to generate cross sections at several fixed collision energies. Each potential surface was treated independently, and total cross sections were obtained by weighting the contribution of each electronic state by 1/3: $\sigma = 1/3[\sigma(^3A') + \sigma(1^3A'') + \sigma(2^3A'')]$. We used standard Monte Carlo methods¹⁴ to generate quasiclassical trajectory (QCT) cross sections, separating contributions into reactive (r) collisions, where the incoming O atom is exchanged with the O atom belonging to the target CO, and inelastic (i) collisions, where the incoming O atom is not exchanged with the O atom belonging to the target CO. For a trajectory to contribute to the inelastic cross section, the final CO(v',j') state must be different than the initial CO(v,j) state. We note that all three electronic states will have significant contributions to the inelastic cross sections. The $2^3A''$ state will in general have only minor contributions to the reactive cross sections because of its repulsive nature. The lowest two electronic states, $^3A'$ and $1^3A''$, will have major contributions to the reactive cross sections because of their low barriers to reaction. All calculations were performed with ^{12}C and ^{16}O atom masses for the target CO and ^{16}O for the

incoming O-atom. The CO mass used in the calculations is therefore slightly different from the experimental measurements, which used $^{16}\text{O} + ^{12}\text{C}^{18}\text{O}$. However, at relative collision velocities of $\sim 8 \text{ km s}^{-1}$, we believe that differences in results arising from the mass difference between $^{12}\text{C}^{16}\text{O}$ and $^{12}\text{C}^{18}\text{O}$ are much smaller than other approximations made in the present calculations. All calculations were done with the target CO in the ground vibrational state and a rotational temperature of 300 K.

We performed two sets of QCT calculations. In one set we focused on obtaining results that could be directly compared to the present measurements. We set the collision velocity to 8 km s^{-1} ($77.9 \text{ kcal mol}^{-1}$). The maximum impact parameter was set to 10 a.u. (5.29 \AA), and 1×10^6 trajectories were run for each of the three electronic states. The value of the maximum impact parameter was made relatively large in order capture the low-angle, low-energy (rotational) scattering in the inelastic channel, which is important when comparing to the present measurements. We calculated differential angular cross sections,

$$\frac{d\sigma}{d\Omega} = \frac{N^{\Delta\theta}}{N_{tot}} \frac{1}{2\pi(\sin\theta)\Delta\theta},$$

where $N^{\Delta\theta}$ is the number of trajectories within the angular bin, $\Delta\theta$, and N_{tot} is the total number of trajectories. To compare with the fine angular resolution of the present measurements, we set $\Delta\theta = 2^\circ$. As discussed in detail later, for the reactive channel, the c.m. scattering angle θ is taken to be the angle between the c.m. velocity vector of the reagent O atom and the c.m. velocity vector of the product CO. For the inelastic channel, θ is the angle between the c.m. velocity vector of the reagent O atom and the c.m. velocity vector of the product O atom. We also calculated c.m. differential translational energy cross sections,

$$\frac{d\sigma}{dE_{trans}} = \frac{N^{\Delta E_{trans}}}{N_{tot}} \frac{1}{\Delta E_{trans}},$$

where $N^{\Delta E_{trans}}$ is the number of trajectories with a final product translational energy, E_{trans} , within an energy bin, ΔE_{trans} . We used an energy bin width of 5.8 kcal mol⁻¹, which approximates the experimental translational energy resolution.

In a second set of QCT calculations, we focused on the collision energy dependence of the rovibrationally resolved cross sections. We performed QCT calculations at O + CO collision velocities of 3, 4, 5, 6, 7, 8, 9, and 10 km s⁻¹, corresponding to c.m. collision energies of 11.0, 19.5, 30.4, 43.8, 59.6, 77.9, 99.6, and 121.7 kcal mol⁻¹, respectively, with the maximum impact parameter set to 5 a.u. (2.65 Å). The maximum impact parameter of 5 a.u. used in these calculations will not be adequate to capture low-angle inelastic scattering resulting in CO(v=0) products (pure rotational transitions). However, these calculations should be sufficient for all reactive collisions and inelastic collisions leading to CO vibrational excitation. In this set of calculations, 2.5×10^5 trajectories were run for each electronic state at each collision energy. This number of trajectories is about a factor of 10 larger than used in our earlier study.⁷ In all calculations, standard histogram binning was used.

B. Theoretical Results. *Results for 8 km s⁻¹ collision velocity.* Figure 2 shows the calculated results for the differential translational energy cross sections for reactive, Eq. (2), and inelastic, Eq. (1), channels of O + CO collisions at a relative velocity of 8 km s⁻¹ (77.9 kcal mol⁻¹). The reactive and inelastic distributions are shown with (solid lines) and without (dashed lines) the contribution of product CO(v=0), to separate the dynamics of pure rotational excitation, which dominates the inelastic channel at high translational energies, from vibrational excitation. The energy bin width is equal to 5.8 kcal mol⁻¹ starting at a center bin of 2.9 kcal

mol^{-1} , so that these theoretical results are directly comparable to the present measured distributions, which have a similar resolution. Distributions obtained after quantum-binning the product $\text{CO}(v,j)$ states, discussed further below, should reveal detailed structure corresponding to rovibrationally resolved CO. We note that the highest energy non-zero cross sections extend to the translational energy bin centered on $83.7 \text{ kcal mol}^{-1}$, which is above the collision energy. Because the reagent CO is at 300 K, some initial rotational energy ends up in product translation for a small fraction of the collisions, and there is some leakage into this high energy bin.

In Fig. 2, a large product translational energy, E_{trans} , corresponds to a low product internal energy. The peak and general behavior at high E_{trans} for the inelastic channel corresponds to mostly pure rotational excitation, and it is typical of non-reactive collisions that occur on a repulsive potential. At lower E_{trans} (higher CO product internal energy), particularly below $E_{\text{trans}} = 40 \text{ kcal mol}^{-1}$, the reactive and inelastic channels have the same broad and flat shape and nearly the same magnitude. The appreciable value of the differential cross section persists to near the zero translational energy cut-off, corresponding to all the available collision energy going into CO internal energy. Also shown are the reactive and inelastic differential translational energy cross sections with the contribution from the product $\text{CO}(v=0)$ removed—i.e., all trajectories where the product CO is in the vibrational ground state do not contribute. The reactive and inelastic channels with the $\text{CO}(v=0)$ contribution removed are nearly identical for all energies and track the full reactive channel (including the $\text{CO}(v=0)$ contribution) differential cross sections below about $E_{\text{trans}} \sim 70 \text{ kcal mol}^{-1}$, which is the approximate threshold for creating vibrationally excited CO. This result implies that the underlying dynamics for collision products where CO is vibrationally excited are similar for both the reactive and inelastic channels.

Figure 3 shows the calculated differential angular cross section for O + CO collisions at 8 km s⁻¹ collision velocity for the reactive, Eq. (2), and inelastic channels, Eq. (1). Results are shown both with (solid lines) and without (dashed lines) the product CO(v=0) contribution, in order to separate pure rotational excitation from rovibrational excitation. Use of a relatively small angular bin width of 2 degrees reveals small rapid oscillations in these curves for smaller values of the cross sections, which is an indication of the statistical uncertainty of these results. In Fig. 3, the large values at low angles for the inelastic channel are typical of low-angle, low-energy-transfer collisions on repulsive surfaces. The peak at low angle for the reactive channel suggests a “stripping” mechanism, where the incoming O-atom strips off a carbon atom from the target CO, and the product CO is scattered mostly forward—i.e., in the same direction as the reagent O-atom velocity vector. Whether it reacts or is scattered inelastically, the reagent O atom is scattered mostly in the same direction as its initial velocity vector. The transition state for reaction is bent, near 120°, which may help explain how the CO reaction product scatters in the same direction as the initial direction of the incoming O atom. The differential angular cross section for the reactive channel is broad as a function of scattering angle, with a small backward peak near 180°. Also shown are the differential angular cross sections without the CO(v=0) contributions. The reactive and inelastic cross sections without the CO(v=0) contributions are again very similar and closely approximate the full reactive differential cross section. It may be that for vibrational excitation, reactive and inelastic trajectories follow similar paths, either on the reagent side of the transition state barrier for inelastic collisions or product side of the transition state barrier for reactive collisions (see Fig. 12 of Braunstein and Duff⁷).

Figures 4a-c show the reactive (Fig. 4a) and inelastic, with (Fig. 4b) and without (Fig. 4c) the product CO(v=0) contribution, rovibrationally resolved cross sections versus the product

translational energy. The values of E_{trans} in these plots were obtained by $E_{\text{trans}} = 77.9 \text{ kcal mol}^{-1} - E_{\text{internal}}(\text{CO}(v,j))$. The numbers in Figs. 4a-c (0-7) correspond to CO(v) level thresholds. (The $\sigma(v,j=0)$ cross sections dip down to very low values and so conveniently indicate vibrational level onsets.) For the inelastic cross sections, Figs. 4b and 4c, much of the $v=0$ cross section is above the scale of the figures. This expression for E_{trans} neglects a small energy contribution from the initial reagent CO internal energy. We note also that the cross section is obtained after binning the classical trajectories into quantum states. Therefore, these finely resolved cross sections cannot be compared quantitatively to the differential translational energy cross sections shown in Fig. 2. However, they are nearly the same quantity, and they reveal rich and detailed state populations. As we shall show, product CO vibrational excitation for $v>10$ and $j>100$ is seen in the calculations. Many of these CO(v,j) states are evident in Fig. 4, but many of the higher (v,j) states overlap the thresholds of higher vibrational manifolds, making these states difficult to distinguish from one another. This rich structure resulting from the highly excited state populations shown in Fig. 4 underlie the results of Fig. 2 and could possibly be revealed in very highly resolved energy measurements. As seen in Fig. 2, the overall magnitude and shape of the inelastic rovibrationally resolved cross sections without the product (CO($v=0$)) contribution, Fig. 4c, closely resembles the full reactive rovibrational distribution, Fig. 4a. The largest differences occur at extremely low E_{trans} (high CO internal energy) where the reactive cross sections remain fairly large up until the $E_{\text{trans}} = 0$ cut-off.

Figure 5 shows the reactive (Fig. 5a) and inelastic (Fig. 5b) rovibrationally resolved cross section $\sigma(\text{CO}(v,j))$, for O + CO collisions at 8 km s^{-1} , for $v=0-3$. We have multiplied the $\sigma(0,j)$ inelastic cross sections by 1×10^{-3} to put these data on a common scale. The rapid oscillations in the other curves are an indication of the statistical uncertainty in the Monte Carlo calculations.

The reactive cross sections for each vibrational level have similar broad shapes, with single maxima, that extend to the maximum available energy, except for $\sigma(0,j)$ which has two maxima, one at high j and one at low j . For $\sigma(v>0,j)$ taken together, the reactive rotational distributions can be fit well with a Boltzmann rotational distribution of $\sim 8,000$ K. (The vibrational temperature is also near 8,000 K.) The rovibrationally resolved cross sections persist to very high rotational quantum numbers, up to $j\sim 110$ (corresponding to ~ 65 kcal mol⁻¹), which is an appreciable fraction of the collision energy of 77.9 kcal mol⁻¹. The inelastic rovibrationally resolved cross sections for product CO($v>0$) have a similar broad shape as the reactive cross sections, extending to $j\sim 100$.

Results at collision velocities from 3 km s⁻¹ through 10 km s⁻¹. To gain more insight into the dynamics, and in anticipation of possible future experiments, Fig. 6 shows the vibrationally resolved cross sections, for O + CO reactive and inelastic collisions at 3, 4, 5, 6, 7, 8, 9, and 10 km s⁻¹ collision velocities. The inelastic $\sigma(v=0)$ cross section is above the scale of the figure. Except for the highest vibrational populations near the available energy limit for a particular collision velocity, the reactive vibrational distributions are similar to Boltzmann distributions. The effective temperatures of these distributions increase with approximately the square of the collision velocity. The inelastic vibrationally resolved cross sections closely resemble the reactive vibrationally resolved cross sections except for $\sigma(v=0)$. For the present energy dependent results, which focus on CO vibrational excitation and where the maximum impact parameter is 5 a.u., the $\sigma(v=0)$ inelastic results will not include significant contributions from large impact parameter, small ΔJ transitions. For vibrationally excited products, the inelastic CO distributions are slightly hotter than the reactive distributions.

Figure 7 examines the average rotational and vibrational energies of product CO, where we show the rotational and vibrational energy fractions, f^j and f^v respectively, for O + CO reactive and inelastic collisions at 3, 4, 5, 6, 7, 8, 9, and 10 km s⁻¹ collision velocities. The rotational and vibrational energy fractions are defined:

$$f^j = \left\langle \frac{E_j}{E_{collision}} \right\rangle = \frac{1}{E_{collision}} \left[\frac{1}{\sigma_{tot}} \sum_j E_j \sigma_j \right]$$

$$f^v = \left\langle \frac{E_v}{E_{collision}} \right\rangle = \frac{1}{E_{collision}} \left[\frac{1}{\sigma_{tot}} \sum_v E_v \sigma_v \right],$$

respectively, where E_j is the rotational energy, E_v is the vibrational energy, $E_{collision}$ is the collision energy, σ_{tot} is the total cross section, $\sigma(j) = \sum_v \sigma(v, j)$, and $\sigma(v) = \sum_j \sigma(v, j)$. The vibrational energy fraction increases with collision energy for the reactive and inelastic channels. The reactive energy fraction shows a rapid increase from threshold, which may reflect the small energy barrier to reaction. The large $\sigma(v=0)$ inelastic cross section makes the overall inelastic vibrational energy fraction, which is an average of the energy of vibrational states, smaller than the reactive energy fraction. The reactive rotational energy fraction is generally flat while the inelastic rotational energy fraction decreases with collision energy. For collision velocities above 8 km s⁻¹, the distribution of internal energy in the elastic channel continues to change, but it remains relatively constant in the reactive channel.

Figure 8 shows two different excitation functions for O + CO collisions: a photon excitation function, σ^p , and a vibrational excitation function, σ^e , both as a function of collision energy. These excitation functions are separated into reactive and inelastic components. We define the photon excitation function as $\sigma^p = \sum_{i=1} i \sigma(v=i)$. The photon excitation function is

particularly convenient for comparisons to laboratory measurements of photon production due to O + CO collisions which integrate signal over the entire fundamental CO band from 4-7 microns, such as the measurements of Upschulte and Caledonia.⁵ The photon excitation function also provides a way to compare directly reactive and inelastic excitation functions by not including CO products formed in the vibrational ground state, which for the inelastic channel would otherwise mask the behavior of the vibrationally excited CO cross section. The photon excitation functions for the reactive and inelastic channels are nearly the same, with the inelastic channel slightly larger. This behavior reflects the similarity of the underlying vibrationally resolved cross sections for excited CO products. We define the vibrational excitation function as $\sigma^e = \sum_{i=1} \sigma(v=i)$. The vibrational excitation functions are also very similar.

III. EXPERIMENTAL DETAILS

A. Methods. The experiments were performed with the use of a crossed-molecular beams apparatus (see Fig. 9) equipped with a fast-atom beam source.^{8,15-18} General details about the experimental apparatus and details of the analysis can be found in an earlier paper.⁸ A pulsed beam of oxygen atoms (¹⁶O) was crossed at right angles with a pulsed, supersonic beam of ¹²C¹⁸O gas. Products that scattered from the interaction region were detected with a rotatable mass spectrometer detector that measured number-density distributions as a function of arrival time at the electron-bombardment ionizer, $N(t)$. These number-density distributions are commonly referred to as time-of-flight (TOF) distributions. Laboratory angular distributions, $N(\theta)$, where θ is the laboratory angle of the scattered products with respect to the O-atom beam, are determined by integrating the TOF distributions over time at a fixed angle for a series of laboratory angles, θ . These data are collected in the laboratory reference frame, so a forward

convolution method^{19,20} is employed to derive center-of-mass (c.m.) quantities from the laboratory TOF and angular distributions.

The hyperthermal beam used in the experiment had an average translational energy of 115 kcal mol⁻¹ (Fig. 10), and the mole fraction of atomic oxygen in the beam was approximately 98 percent. The hyperthermal ¹⁶O-atom beam was crossed at a 90° intersection angle by a pulsed beam of isotopically-labeled carbon monoxide molecules (C¹⁸O). The C¹⁸O (Isotec, Sigma Aldrich) was 98.7% C¹⁸O, with the remainder (1.3%) being C¹⁶O. A supersonic expansion of C¹⁸O was created with a piezoelectric pulsed valve from a stagnation pressure of 10 psig C¹⁸O. The C¹⁸O beam passed through a 5-mm-diameter skimmer and a 3-mm-diameter aperture before crossing the O-atom beam. The distance between the nozzle and skimmer was 9.2 cm, and the distance from the skimmer to the 3-mm-diameter aperture was 2.8 cm. From the aperture, the beam traveled 1.5 cm to the crossing point of the two beams. The C¹⁸O beam velocity was estimated to be 800 ± 80 m s⁻¹.²¹ The velocity of the C¹⁸O beam was an order of magnitude lower than the O-atom beam, and the velocity width of the C¹⁸O beam was not considered in the analysis of the experimental data. The crossing region of the two beams was located 99 cm from the apex of the conical nozzle of the O-atom source and 13 cm from the orifice of the C¹⁸O pulsed valve source.

The collision-energy distribution in the c.m. reference frame was derived from the O-atom beam-velocity distribution (related to Fig. 10 by $E_{\text{trans}} = \frac{1}{2} m v^2$) and the nominal velocity of the carbon monoxide beam using the equation, $E_{\text{coll}} = \frac{1}{2} \mu v_{\text{rel}}^2$, where μ is the reduced mass and v_{rel} is the relative velocity of the O atoms and the C¹⁸O molecules. The average collision energy in this experiment was 83 kcal mol⁻¹, and the width of the collision-energy distribution (FWHM) was ~30 kcal mol⁻¹, ranging from 70 to 100 kcal mol⁻¹. A Newton diagram for collisions of O

atoms and $C^{18}O$ with $E_{\text{coll}} = 83 \text{ kcal mol}^{-1}$ is shown in Fig. 11. This diagram shows maximum recoil velocities for inelastically-scattered $C^{18}O$ (solid blue circle) and ^{16}O (dashed blue circle). It also shows maximum recoil velocities for reactively-scattered ^{16}OC (solid red circle) and ^{18}O (dashed red circles). The shaded region shown on the Newton diagram indicates the range of laboratory angles used for the experiment: 6° to 54° with respect to the nominal velocity vector of the hyperthermal O-atom beam.

The experiments focused on the reactively-scattered ^{16}OC molecules ($m/z = 28$), inelastically-scattered $C^{18}O$ molecules ($m/z = 30$), and inelastically-scattered O atoms ($m/z = 16$). Signals from $m/z = 32$ (O_2^+) were used to correct the $m/z = 16$ data for the contribution of inelastically scattered O_2 cracking to O^+ on the ionizer. Low signals combined with high background levels of water in the detector at $m/z = 18$ made it impossible to detect the reactive ^{18}O product. TOF distributions were collected for 2000 beam pulses for $m/z = 28$ ($^{16}OC^+$) and 30 ($C^{18}O^+$), and 200 beam pulses for 16 (O^+), and 32 (O_2^+) at each laboratory angle. The laboratory angle was adjusted in 2 degree increments until the entire angular range was covered. Then the increment direction was reversed and the cycle was repeated until a total of four TOF distributions had been collected for each product at each detector angle. Because this process lasted more than 35 hours, it was important to sum the TOF distributions collected in this manner to account for minor long-term drifts in the experimental parameters. At a representative laboratory angle of 10° , the integrated count rates were $8.5 \times 10^6 \text{ counts s}^{-1}$ for $m/z = 30$ ($C^{18}O^+$), $1.2 \times 10^8 \text{ counts s}^{-1}$ for $m/z = 16$ (O^+), and $2.5 \times 10^7 \text{ counts s}^{-1}$ for $m/z = 28$ ($^{16}OC^+$).

B. Experimental Results. Inelastic scattering. Figure 12 shows TOF distributions for $m/z = 16$ (O^+) and 30 ($C^{18}O^+$) collected at five representative laboratory detector angles. Figure 13 shows laboratory angular distributions for inelastically scattered O and $C^{18}O$. The curves in

Figs. 12 and 13 are the forward-convolution fits to the laboratory angular distributions for the O product (red) and the C¹⁸O product (blue), based on the c.m. translational energy and angular distributions in Fig. 14. The distributions shown in Fig. 14 are taken from the theoretical results in Figs. 2 and 3 but presented on a linear scale. These calculated c.m. distributions accurately predict the laboratory distributions, as seen in Figs. 12 and 13. The O product is forward scattered and the C¹⁸O is backward scattered with respect to the initial direction of the reagent O atoms in the c.m. frame. The laboratory detection angles are primarily sensitive to C¹⁸O molecules that scatter into the backward hemisphere in the c.m. reference frame with respect to the direction of the incident O atoms (see Fig. 11), so only the angular range in the c.m. angular distributions that was accessible in experiment was used in the forward convolution. The experiments were sensitive to C¹⁸O and O scattered from 0° to 120° and from 0° to 80°, respectively, in the c.m. reference frame. The translational energy distribution reveals that, on average, about 85% of the available energy (83 kcal mol⁻¹) is released in translation in the inelastic channel, although there is a tail to low translational energies suggesting that some collisions result in large energy transfers to internal degrees of freedom of C¹⁸O. The angular distributions of scattered O and C¹⁸O illustrate the propensity for forward scattering which results from high-impact-parameter collisions.

Although the hyperthermal beam in our experiment had only two percent O₂, the inelastic cross section for O₂ + C¹⁸O is almost twice that for O + C¹⁸O, so the contribution to the inelastic scattering signal detected at $m/z = 30$ (C¹⁸O⁺) was not beneath our detection limits. A second inelastic scattering process, O₂ + C¹⁸O → C¹⁸O + O₂ was identified as a small, fast shoulder in the TOF distributions collected at $m/z = 30$ (C¹⁸O⁺). A functional form for the fast component was determined, and this component was subtracted from all the TOF distributions collected at

$m/z = 30$ ($C^{18}O^+$), including those shown in Fig. 12. Only the slower (main) peak, corresponding to the $C^{18}O$ that scattered inelastically from ^{16}O , was used to gather dynamical information about the inelastic channel.

Reactive scattering. TOF distributions collected at $m/z = 28$ ($^{16}OC^+$) at five representative laboratory angles are shown in Fig. 15, and the corresponding laboratory angular distribution is shown in Fig. 16. Center-of-mass angular and translational energy distributions for the $O(^3P) + C^{18}O \rightarrow ^{16}OC + ^{18}O$ reaction were obtained from the QCT calculations and are shown as dashed blue curves in Fig. 17. These c.m. distributions were used in the forward-convolution procedure to predict laboratory TOF and angular distributions shown as dashed blue curves in Figs. 15 and 16. The TOF distributions, predicted from the theoretical c.m. translational energy and angular distributions, match the experimental distributions very well, but the predicted laboratory angular distribution does not quite match the observed flux difference between forward and sideways scattering in the laboratory angular distribution. The experimentally derived c.m. translational energy and angular distributions are shown as red curves in Fig. 17. These experimental curves were obtained by optimizing a translational energy distribution, based on an RRK form²², and an angular distribution of arbitrary point form. The corresponding laboratory TOF and angular distributions are shown as the solid red curves in Figs. 15 and 16. The theoretically calculated translational energy distribution exhibited some structure, but the experimental resolution did not justify adding structure to the experimentally derived translational energy distribution. Thus, within experimental error, both the theoretical and experimental translational energy distributions may be the same. The difference between the theoretical and experimental c.m. angular distributions is believed to be just outside experimental error. The theoretical and experimental results both indicate that about 60% of the available

energy is released in translation and that the $^{16}\text{O}^{16}\text{C}$ product is predominantly forward scattered. The theoretical calculations predict a small increase in the amount of $^{16}\text{O}^{16}\text{C}$ scattering at the most backward angles, near 180° , but that angular range is beyond the range to which the experiment is sensitive. A velocity-flux map, shown in Fig. 18, illustrates the differential scattering cross section of the reactive $^{16}\text{O}^{16}\text{C}$ product, where $^{16}\text{O}^{16}\text{C}$ tends to be forward scattered, with a broad range of product velocities. In the angular range probed by the experiment, the theoretical and experimental results for this channel are in almost quantitative agreement, with only a slight discrepancy in the angular distribution.

IV. DISCUSSION

The experimentally observed inelastic scattering data is predicted quantitatively by the theoretical c.m. translational energy and angular distributions. As expected for inelastic collisions, O atoms scatter from CO with little change in direction and velocity. Thus, the O atoms are predominantly forward scattered and the CO molecules are predominately backward scattered in the c.m. reference frame. And the c.m. translational energy distribution has a maximum near the c.m. collision energy. Subtracting the translational energy distribution from the collision energy gives the internal energy distribution of scattered CO. On average, ~15 percent of the collision energy is transferred into internal energy. However, the low-energy tail in the translational energy distribution indicates that a large fraction (~84 percent) of single $\text{O}(^3P) + \text{CO}$ collisions can transfer more than ~6 kcal mol $^{-1}$ into internal energy in the CO, corresponding to greater than one quanta of vibration ($v=1$). A smaller fraction (~0.5 percent) of scattered CO molecules may have more than ~63 kcal mol $^{-1}$ of internal energy, corresponding to CO ($v=11$). Although the majority of inelastic collisions lead to CO that is scattered in the

backward direction with respect to the initial direction of the reagent O atoms, it should be noted that $C^{18}O$ detected in the experiment can only come from collisions of O atoms with $C^{18}O$ molecules that lead to $C^{18}O$ scattering in the forward direction with respect to the reagent O atoms (refer to Newton diagram in Fig. 11). The forward scattered CO could be the result of low-impact-parameter collisions. Large energy transfers have been observed when hyperthermal Ar atoms scatter from C_2H_6 or C_2F_6 at low impact parameters;^{15,23} however, in analyzing the calculated O + CO trajectories, it was difficult to conclude that low-impact-parameter collisions were necessarily correlated with large energy transfers. Instead, large energy transfers in inelastic collisions seem to be correlated with failed reactive collisions (see below).

An analysis of the experimental results suggests that roughly ten percent of the collisions of O(3P) with CO at $\langle E_{\text{coll}} \rangle = 83 \text{ kcal mol}^{-1}$ lead to an O-atom exchange reaction, detected by the observation of scattered ^{16}OC . Assuming a typical hard-sphere cross section of $\sim 10^{-15} \text{ cm}^2$, this experimental result would suggest a total reactive cross section, $\sum_{i=0} \sigma^r(v=i)$, of $\sim 10^{-16} \text{ cm}^2$.

This value is in rough agreement with the present QCT calculated total reactive cross section of $1.98 \times 10^{-16} \text{ cm}^2$. This rough agreement would seem to support the conclusion that the vibrational excitation cross section magnitudes reported earlier by Upschulte and Caledonia⁵ and Green et al.⁶ are too low by about an order of magnitude. Within experimental uncertainty, the theoretically calculated and experimentally observed c.m. translational energy distributions for reactive collisions (see Fig. 17) are identical, suggesting a broad range of product translational energies with an average of 60 percent of the available energy (i.e., the collision energy) released in translation. The theoretically calculated c.m. angular distribution is very similar to the experimentally derived angular distribution (see Fig. 17), but these two distributions are not quite in quantitative agreement. The experimental result predicts slightly more forward scattering of

OC relative to sideways scattering than does the theoretical result. The slight disagreement in the c.m. angular distributions might reflect a minor error in the OCO potential or, perhaps, the fact that the calculations employed a classical rather than quantum scattering treatment. The good agreement between the experimental results and the predictions of the QCT calculations, which used only the three low-lying triplet potential energy surfaces, suggests that intersystem crossing does not play a role in the dynamics of $O(^3P) + CO$ collisions. The absence of intersystem crossing was also a conclusion in the measurements of the excitation functions for $O(^3P) + H_2 \rightarrow OH + H$,²⁴ and $O(^3P) + CH_4 \rightarrow OCH_3 + H$,⁹ and in the dynamics of the reaction $O(^3P) + D_2 \rightarrow OD + D$.⁸ The c.m. translational energy distributions show that reactively scattered OC tends to be highly internally excited. On average, the reactive OC products are formed with internal energies corresponding to roughly $v=5$ or $v=6$. But a significant fraction (~8 percent) are formed with internal energies corresponding to $v=11$ or higher. The propensity of reactive OC products to scatter in the forward direction might be interpreted as a manifestation of a stripping reaction, in which the reaction occurs through high-impact-parameter collisions. However, a typical characteristic of a stripping mechanism is relatively little energy transfer into product internal degrees of freedom, which is at odds with the observation of large energy transfers.

Examination of the calculated trajectories provides insight into the mechanism that leads to the observed scattering dynamics. Several examples of animated trajectories may be viewed online as Supporting Information. With the exception of the large-impact-parameter collisions that lead to inelastic scattering with little change in direction and velocity, the collisions that lead to both inelastic and reactive products have a striking similarity. This was shown earlier in the extremely high degree of similarity of the theoretically calculated angular and translational

energy distributions for the inelastic and reactive channels without the CO($v=0$) contribution. The shallow wells of the two lowest lying potential energy surfaces facilitate the formation of a transient OCO complex, which is formed over a large range of impact parameters but mainly for angles of approach that are close to the transition state geometry (O–C–O angle of $\sim 120^\circ$). The complex can persist for several vibrational periods, but it usually does not last long enough for a rotational period. Once the complex is formed, the outcome may be an exchange of the O atom that is bound to the C atom (reactive scattering) or no exchange (inelastic scattering). Such a complex trajectory that results in inelastic scattering may be thought of as a failed reactive collision. Thus, for reactive scattering trajectories and for inelastic scattering trajectories that transfer significant energy to the CO product, the collisions involve a complex that tends to channel CO products into the forward direction but that can also fling CO products into the sideways and backward directions. The details of how the complex falls apart determine whether or not the outcome is reactive or inelastic and how the energy is partitioned into product degrees of freedom. The theoretical observation of a transient OCO complex supports earlier suggestions of such a complex that can be stabilized by collisions, in connection with isotopic fractionation of CO₂ in the atmosphere.²⁵

The theoretical calculations provide a detailed view of the rotational and vibrational excitation in the CO products. Figure 5 shows that the reactive and inelastic rovibrationally resolved cross sections extend to $j \sim 100$. The $\sigma(0,j)$ inelastic cross section peaks at much lower rotational quantum numbers and has a much larger magnitude, reflecting the different dynamics of pure rotational excitation, which occurs at large impact parameters. The maxima for the inelastic $\sigma(v=1-3,j)$ cross sections occur for lower rotational quantum numbers as the vibrational levels increase, reflecting the fact that less energy is available for rotation as the vibrational

excitation increases. This trend is in agreement with previous experimental studies of reactive triatomic collisions,²⁶ and for experimental²⁷ and theoretical studies^{28,29} on inelastic triatomic collisions. In general, products can be highly rotationally excited, especially when the product vibrational energy is relatively low.

As an independent validation of the calculated rovibrational distributions, we show in Fig. 19 calculated nascent emission spectra based on the CO(v,j) populations for the summed reactive and inelastic channels and measured nascent spectra for O + CO collisions near 8 km s⁻¹ relative velocity. The calculated spectra were generated from the combined inelastic and reactive CO(v,j) populations and tabulated lifetimes for CO(v,j) states. Fig. 19a shows the calculated results at 5.0 cm⁻¹ resolution from 2 to 7 microns, where $\Delta v=1$ (fundamental) and $\Delta v=2$ (overtone) bands are clearly visible. We note the bandhead structure in the fundamental and overtone spectra corresponding to R-branch transitions from high rotational levels ($j=50-100$) in excited vibrational levels of CO. Within the fundamental band, each peak corresponds to an R-branch transition from a particular vibrational level, with the shortest wavelength peak corresponding to transitions from $v=1$, and so on. Fig. 19b shows the same calculated nascent spectra degraded to 0.05 microns spectral resolution. Fig. 19b also shows results from two measurements, the crossed-beams laboratory measurements of Upschulte and Caledonia,¹¹ which range from 4.5 – 5.5 microns, and the space-based orbital gas release measurements of Green *et al.*¹⁴ (digitized from Fig. 12, 17933 scan), which range from 2-7 microns. The Green *et al.* spectra capture the fundamental and overtone emission. All spectra have been normalized so that their maxima are 1.0. The spectrum of Upschulte and Caledonia was shifted by -0.848 microns and the spectrum of Green *et al.* was shifted by +0.0772 microns. There is very good agreement between all spectra for the fundamental band, except at longer wavelengths where the

spectrum of Green *et al.* has apparently a low signal to noise ratio. The ratio of the overtone to the fundamental peak heights for the calculated spectrum is about 1.5 larger than the measured spectrum of Green *et al.* This difference may be the result of uncertainties in combining spectra from two different circular variable filters (CVFs) covering different wavelength regions (0.7-5 microns and 4.7-22 microns), other uncertainties involving the absolute determination of relative velocities of O and CO, the sensitivity of the measured spectrum to the direction of the CVF field of view, other factors in these difficult space measurements, or in deficiencies in the present calculations. More highly resolved spectra are required to determine the origins of these differences.

The current experimental and theoretical results reveal similar limits in the amount of internal excitation in scattered CO to what was reported in the IR emission experiment conducted by Upschulte and Caledonia.⁵ They concluded that collisions of O(³P) with CO at $E_{\text{coll}} = 77.9$ kcal mol⁻¹ can produce CO in vibrational levels up to $v=11$, while our crossed-beams study of O(³P) with C¹⁸O at $\langle E_{\text{coll}} \rangle = 83$ kcal mol⁻¹ verified that both the inelastic product, C¹⁸O, and the reactive product, ¹⁶OC, may be in vibrational levels of $v=11$ or greater. A high degree of consistency is emerging between the present measurements, the spectral measurements of Caledonia and Upschulte, the spectral measurements of Green *et al.*, and the theoretical calculations, especially with regard to the high degree of internal excitation of the product CO.

V. CONCLUDING REMARKS

Crossed-molecular beams methods and theoretical calculations have been used to investigate the hyperthermal interactions of O(³P) with CO at c.m. collision energies near 83 kcal mol⁻¹ (corresponding to a relative velocity near 8 km s⁻¹). Inelastic scattering experiments

on the process, $^{16}\text{O}(^3P) + \text{C}^{18}\text{O}(v,j) \rightarrow \text{C}^{18}\text{O}(v',j') + ^{16}\text{O}$, indicate that oxygen atoms mainly scatter from C^{18}O with relatively large impact parameters and lead to forward scattering with little change in direction and translational energy. Averaged over all inelastic collisions, ~15 percent of the collision energy is transferred to internal energy in CO. Although this fraction is relatively small, the collision energy is high, so internal excitation of CO above an energy corresponding to $v=1$ still occurs in approximately 84 percent of all inelastic collisions. The reactive channel, $^{16}\text{O}(^3P) + \text{C}^{18}\text{O} \rightarrow ^{16}\text{OC} + ^{18}\text{O}$, created ^{16}OC products that are frequently scattered in the forward direction, although the fraction of collisions that lead to ^{16}OC scattered in the forward direction is comparable to the fraction that lead to sideways and backward scattering. The ^{16}OC product formed in the reactive channel had a very broad translational energy distribution, with ~40 percent, on average, of the available (collision) energy transferred into internal excitation. Approximately 97 percent of reactive collisions produce ^{16}CO with internal energies greater than an energy corresponding to $v=1$, and about 8 percent of collisions lead to internal energies greater than $v=11$. Quasiclassical trajectory calculations on computed triplet potential energy surfaces are in excellent agreement with the experimental results. The calculations reveal a mechanism for large energy transfers, into both rotation and vibration, where the reagent O atom encounters the carbon end of the CO molecule a range of impact parameters in a bent O–C–O geometry (~80°–140°). The three atoms linger together for less than a rotational period but usually for more than a CO vibrational period, and the transient complex breaks up into either inelastic or reactive products. The inelastic trajectories that lead to significant energy transfer to the CO may thus be considered failed reactive collisions. The similarity in inelastic and reactive trajectories that lead to high vibrational excitation in the CO product is supported by calculated translational energy and angular distributions for reactive and

inelastic collisions without the $\text{CO}(v=0)$ product. These distributions, which remove contributions from purely inelastic rotational excitation, are nearly identical. The theoretical calculations have been used to predict inelastic and reactive cross sections at a variety of collision energies and to predict infrared emission spectra that compares favorably with earlier measurements. Given the accuracy with which the calculations predict the collision dynamics observed in our high-fidelity crossed-beams experiments, we expect the mechanistic insights and additional predictions offered by the theory to be accurate, too.

ACKNOWLEDGEMENTS

This work was supported by the Small Business Innovative Research (SBIR) program of the Missile Defense Agency (MDA), Contract No. F04611-03-C-0015 (technical oversight from Dr. Marty Venner), by the MDA under Cooperative Agreement HQ0006-05-2-0001, and by the Department of Defense Experimental Program for the Stimulation of Competitive Research (DEPSCoR), administered by the Air Force Office of Scientific Research (Grant No. FA9550-04-1-0428). The authors acknowledge helpful technical discussions with P. Zittel and W. Dimpfl of Aerospace Corporation and L. Bernstein of Spectral Sciences, Inc. Amy L. Brunsvold is grateful for fellowships from the Zonta Foundation and the Montana Space Grant Consortium.

SUPPORTING INFORMATION

Representative animated trajectories of $\text{O} + \text{CO}$ collisions are available as Supporting Information. These trajectories represent exchange of the oxygen atom that is bound to the carbon atom (reactive scattering) and collisional excitation of CO without exchange of the oxygen atom (inelastic scattering). Some trajectories show the formation of a transient complex

in which the three atoms linger together for a short time, usually less than a rotational period, before separating into products. This material is available free of charge via the Internet as a Link associated with the manuscript.

REFERENCES

- (1) English, L. K. *Mat. Eng.* **1987**, *104*, 39.
- (2) Hunton, D. E. *Sci. Am.* **1989**, *261*, 92.
- (3) Minton, T. K.; Garton, D.J. Chemical Dynamics in Extreme Environments. In *Advanced Series in Physical Chemistry* Dressler, R. A., Ed.; World Scientific: Singapore, 2001; Vol. 11; pp 420.
- (4) Murad, E. *J. Spacecraft and Rockets* **1996**, *33*, 131.
- (5) Upschulte, B. L.; Caledonia, G. E. *J. Chem. Phys.* **1992**, *96*, 2025.
- (6) Green, B. D.; Holtzclaw, K. W.; Joshi, P. B.; Burke, H. K. *J. Geophys. Res.* **1992**, *97*, 12161.
- (7) Braunstein, M.; Duff, J. W. *J. Chem. Phys.* **2000**, *112*, 2736.
- (8) Garton, D. J.; Brunsvold, A. L.; Minton, T. K.; Troya, D.; Maiti, B.; Schatz, G. C. *J. Phys. Chem. A.* **2006**, *110*, 1327.
- (9) Troya, D.; Schatz, G. C.; Garton, D. J.; Brunsvold, A. L.; Minton, T. K. *J. Chem. Phys.* **2004**, *120*, 731.
- (10) Braunstein M.; Wysong, I. J., "Direct Simulation Monte Carlo Modeling of High Energy Chemistry in Molecular Beams: Chemistry Models and Flowfield Effects," *22nd International Rare Gas Dynamics Conference, Sydney Australia, July, 2000*.
- (11) Inn, E. C. Y.; Watanabe, K.; Zelikoff, M. *J. Chem. Phys.* **1953**, *21*, 1648.
- (12) Schmidt, M. W.; Baldrige, K. K.; Boatz, J. A.; Elbert, S. T.; Gordon, M. S.; Jensen, J. H.; Koseki, S.; Matsunaga, N.; Nguyen, K. A.; Su, S. J.; Windus, T. L.; Dupuis, M.; Montgomery, J. A. *J. Comput. Chem.* **1993**, *14*, 1347.
- (13) Aguado, A.; Paniagua, M. *J. Chem. Phys.* **1992**, *96*, 1265.

- (14) Truhlar, D. G.; Muckerman, J. T. *Atom-Molecule Collision Theory*; Plenum Press: New York, 1979.
- (15) Brunsvold, A. L.; Garton, D. J.; Minton, T. K.; Troya, D.; Schatz, G. C. *J. Chem. Phys.* **2004**, *121*, 11702.
- (16) Lee, Y. T.; McDonald, J. D.; Lebreton, P. R.; Herschbach, D. R. *Rev. Sci. Instrum.* **1969**, *40*, 1402.
- (17) O'Loughlin, M. J.; Reid, B. P.; Sparks, R. K. *J. Chem. Phys.* **1985**, *83*, 5647.
- (18) Zhang, J. M.; Garton, D. J.; Minton, T. K. *J. Chem. Phys.* **2002**, *117*, 6239.
- (19) Buss, R. J., Ph.D. Thesis, University of California, Berkeley, 1979.
- (20) Lee, Y. T. Reactive Scattering I. Nonoptical Methods. In *Atomic and Molecular Beam Methods*; Scoles, G., Ed.; Oxford University Press: New York, NY, 1988; Vol. 1; pp 553.
- (21) Auerbach, D. J. Velocity Measurements by Time-of-Flight Methods. In *Atomic and Molecular Beam Methods*; Scoles, G., Ed.; Oxford University Press: New York, NY, 1988; Vol. 1; pp 362.
- (22) Schatz, G. C. *J. Chem. Phys.* **1985**, *83*, 5677.
- (23) Tasic, U.; Hein, P.; Troya, D. *J. Phys. Chem. A.* **2007** *111*, 3618.
- (24) Garton, D. J.; Minton, T. K.; Maiti, B.; Troya, D.; Schatz, G. C. *J. Chem. Phys.* **2003**, *118*, 1585.
- (25) Pandey, A.; Bhattacharya, S. K. *J. Chem. Phys.* **2006**, *124*, 234301; *J. Chem. Phys.* **2006** *125*, 149903.
- (26) Chapman, W. B.; Blackmon, B. W.; Nizkorodov, S.; Nesbitt, D. J. *J. Chem. Phys.* **1998**, *109*, 9306.
- (27) Lindner, J.; Lundberg, J. K.; Lovejoy, C. M.; Leone, S. R. *J. Chem. Phys.* **1997**, *106*, 2265.
- (28) Aker, P. M.; Valentini, J. J. *J. Phys. Chem.* **1993**, *97*, 2078.
- (29) Schatz, G. C. *J. Chem. Phys.* **1997**, *106*, 2277.

FIGURE CAPTIONS

Figure 1. Calculated potential energy curves of the ground singlet state of CO₂, (¹A'), and the three lowest triplet states, ³A', 1 ³A'', and 2 ³A'', at an O–C–O angle of 120° and where one of the C–O bond distances is fixed at 1.2 Å and the other is varied. The curves show these states, at C_s geometries to their O + CO dissociation limits, as a function of the variable C–O distance, R_{CO}.

Figure 2. Calculated differential energy cross sections, $d\sigma/dE_{\text{trans}}$, for O + CO collisions at 8 km s⁻¹ collision velocity ($E_{\text{coll}} = 77.9 \text{ kcal mol}^{-1}$). — (black line) total reactive channel, — (red line) total inelastic channel, ---- (black dotted line) total reactive minus contribution from reactive CO(v=0) product, ---- (red dotted line) total reactive minus contribution from reactive CO(v=0) product.

Figure 3. Calculated differential angular cross sections, $d\sigma/d\Omega$, for O + CO collisions in the c.m. frame at 8 km s⁻¹ collision velocity ($E_{\text{coll}} = 77.9 \text{ kcal mol}^{-1}$). — (black line) total reactive channel; — (red line) total inelastic channel, ---- (black dotted line) total reactive minus contribution from reactive CO(v=0) product, ---- (red dotted line), total reactive minus contribution from reactive CO(v=0) product. For the reactive channel, the c.m. scattering angle, Θ_{cm} , is defined as the inverse cosine of the dot product of the unit velocity vectors in the c.m. frame of the incoming (reagent) O-atom and outgoing (product) CO molecule. For the inelastic channel, the c.m. scattering angle, Θ_{cm} , is defined as the inverse cosine of the dot product of the unit velocity vectors in the c.m. frame of the incoming (reagent) O atom and outgoing (product) O atom.

Figure 4. Calculated cross sections for O + CO collisions at 8 km s⁻¹ collision velocity ($E_{\text{coll}} = 77.9 \text{ kcal mol}^{-1}$), showing the contribution from each final CO(v,j) state as a function of the final translational energy of collision products. (a) reactive channel, (b) inelastic channel, (c) inelastic channel minus the CO(v=0,j) product contributions. The numbers in the figures indicate the thresholds for the CO(v) product vibrational levels. In (b), the contribution from CO(v=0) below the CO(v=1) threshold extends above the axis limit and so is not visible in the figure.

Figure 5. Calculated rovibrationally resolved cross sections for O + CO collisions at 8 km s⁻¹ collision velocity ($E_{\text{coll}} = 77.9 \text{ kcal mol}^{-1}$). (a) reactive channel, (b) inelastic channel. — (black line) CO(v=0), — (red line) CO(v=1), — (blue line) CO(v=2), — (green line) CO(v=3). The CO(v=0) inelastic cross section has been multiplied by 1×10^{-3} in order to fit on the scale.

Figure 6. Calculated vibrationally resolved cross sections for O + CO collisions at 3, 4, 5, 6, 7, 8, 9, 10 km s⁻¹ collision velocities. (a) reactive collisions, (b) inelastic collisions. The numbers in the figure refer to the collision velocity.

Figure 7. Calculated CO product energy fractions for O + CO collisions as a function of collision energy. ○ reactive channel, □ inelastic channel, — vibrational energy fraction (f^v), ---- rotational energy fraction (f^j).

Figure 8. Calculated vibrational excitation and photon cross sections for O + CO collisions as a function of collision energy. ○ reactive channel, □ inelastic channel, — results for the photon cross section $\sigma^p = \sigma(v=1) + 2\sigma(v=2) + 3\sigma(v=3) + \dots$, ---- results for the vibrational excitation function $\sigma^e = \sigma(v=1) + \sigma(v=2) + \sigma(v=3) + \dots$.

Figure 9. Pictorial diagram of the crossed molecular beams apparatus.

Figure 10. Translational energy distributions of atomic and molecular oxygen in the hyperthermal beam. The mole fraction of O atoms is 98 percent, and the mole fraction of O₂ molecules is 2 percent.

Figure 11. Newton diagram for collisions of O(³P) with C¹⁸O at $E_{\text{coll}} = 83 \text{ kcal mol}^{-1}$, where O has a velocity of 8100 m s⁻¹ and the C¹⁸O beam velocity is 800 m s⁻¹. The shaded region indicates the range of laboratory angles examined. The radii of the blue circles represent the recoil velocities of elastically scattered C¹⁸O (solid) and ¹⁶O (dashed). The radii of the red circles represent the maximum recoil velocities of reactively scattered ¹⁶OC (solid) and ¹⁸O (dashed).

Figure 12. Time-of-flight distributions of inelastically scattered O and C¹⁸O following collisions with $\langle E_{\text{coll}} \rangle = 83 \text{ kcal mol}^{-1}$. The circles are the experimental data. The red (O) and blue (C¹⁸O) solid curves are the forward-convolution simulations of the data, derived from the c.m. angular and translational energy distributions of corresponding colors in Fig. 14.

Figure 13. Laboratory angular distributions of O atoms and C¹⁸O molecules that scattered inelastically with $\langle E_{\text{coll}} \rangle = 83 \text{ kcal mol}^{-1}$. The circles with error bars are the experimental data, and the colored lines are the forward-convolution fits to the data, derived from the c.m. angular and translational energy distributions of corresponding colors in Fig. 14. The error bars are estimated from fitting the experimental TOF distributions with a modified Gaussian function and

finding areas of the maximum and minimum acceptable fits by adjusting the Gaussian parameters. The error bars thus represent the maximum and minimum integrals of the TOF distributions based on our best judgment and are expected to be greater than $\pm 2\sigma$.

Figure 14. Center-of-mass angular and translational energy distributions for the inelastic scattering of O with $C^{18}O$ at $\langle E_{\text{coll}} \rangle = 83 \text{ kcal mol}^{-1}$, used in the forward-convolution fit of the laboratory TOF and angular distributions for $m/z = 16$ (O^+) and 30 ($C^{18}O^+$). These distributions were obtained from QCT calculations for O (red) and $C^{18}O$ (blue).

Figure 15. Time-of-flight distributions of reactively scattered ^{16}OC following reaction of $O(^3P)$ with $C^{18}O$ at $\langle E_{\text{coll}} \rangle = 83 \text{ kcal mol}^{-1}$. The circles are the experimental data. The dashed blue and solid red curves are the forward-convolution simulations of the data, derived from the c.m. angular and translational energy distributions of corresponding colors in Fig. 17. The dashed blue curves are predicted by theory, and the solid red curves are the results from optimizing the c.m. distributions (shown in Fig. 17) to fit the data. The experimental (solid red) and the theoretical (dashed blue) curves are nearly identical for each TOF distribution.

Figure 16. Laboratory angular distribution (circles with error bars) of the reactively scattered ^{16}OC product following reaction of $O(^3P)$ with $C^{18}O$ at $\langle E_{\text{coll}} \rangle = 83 \text{ kcal mol}^{-1}$. The dashed blue and solid red curves are the forward-convolution simulations of the data, derived from the c.m. angular and translational energy distributions of corresponding colors in Fig. 17. The dashed blue curve is predicted by theory, and the solid red curve is the result from optimizing the c.m. distributions (shown in Fig. 17) to fit the data. The error bars are estimated from fitting the experimental TOF distributions with a modified Gaussian function and finding areas of the maximum and minimum acceptable fits by adjusting the Gaussian parameters. The error bars thus represent the maximum and minimum integrals of the TOF distributions based on our best judgment and are expected to be greater than $\pm 2\sigma$.

Figure 17. Center-of-mass angular and translational energy distributions for reactive scattering of $O(^3P)$ with $C^{18}O$ at $\langle E_{\text{coll}} \rangle = 83 \text{ kcal mol}^{-1}$, used in the forward-convolution fit of the laboratory TOF and angular distributions for $m/z = 28$ ($^{16}OC^+$). The angular distribution (left) pertains to the reactively scattered ^{16}CO . The distributions shown in dashed blue were obtained from QCT calculations, and those shown in red were determined by optimizing the c.m. distributions to fit the data.

Figure 18. (a) Experimental and (b) theoretical c.m. velocity-flux maps for the reactive ^{16}OC product, derived from the angular and translational energy distributions shown in Fig. 17.

Figure 19. Infrared emission spectra from nascent CO after hyperthermal O + CO collisions. (a) Calculated spectrum at 5 cm^{-1} spectral resolution for collisions at 8 km s^{-1} collision velocity

($E_{\text{coll}} = 77.9 \text{ kcal mol}^{-1}$). (b) — calculated spectrum as in (a) degraded to $0.05 \mu\text{m}$ spectral resolution, •-•- measured spectrum from Green *et al.*⁶, ----- measured spectrum of Upschulte and Caledonia.⁵ The spectrum of Green *et al.*⁶ has been shifted by $+0.0772 \mu\text{m}$, and the spectrum of Upschulte and Caledonia⁵ has been shifted by $-0.0848 \mu\text{m}$. All spectra are normalized so that the maximum intensity value is 1.0.

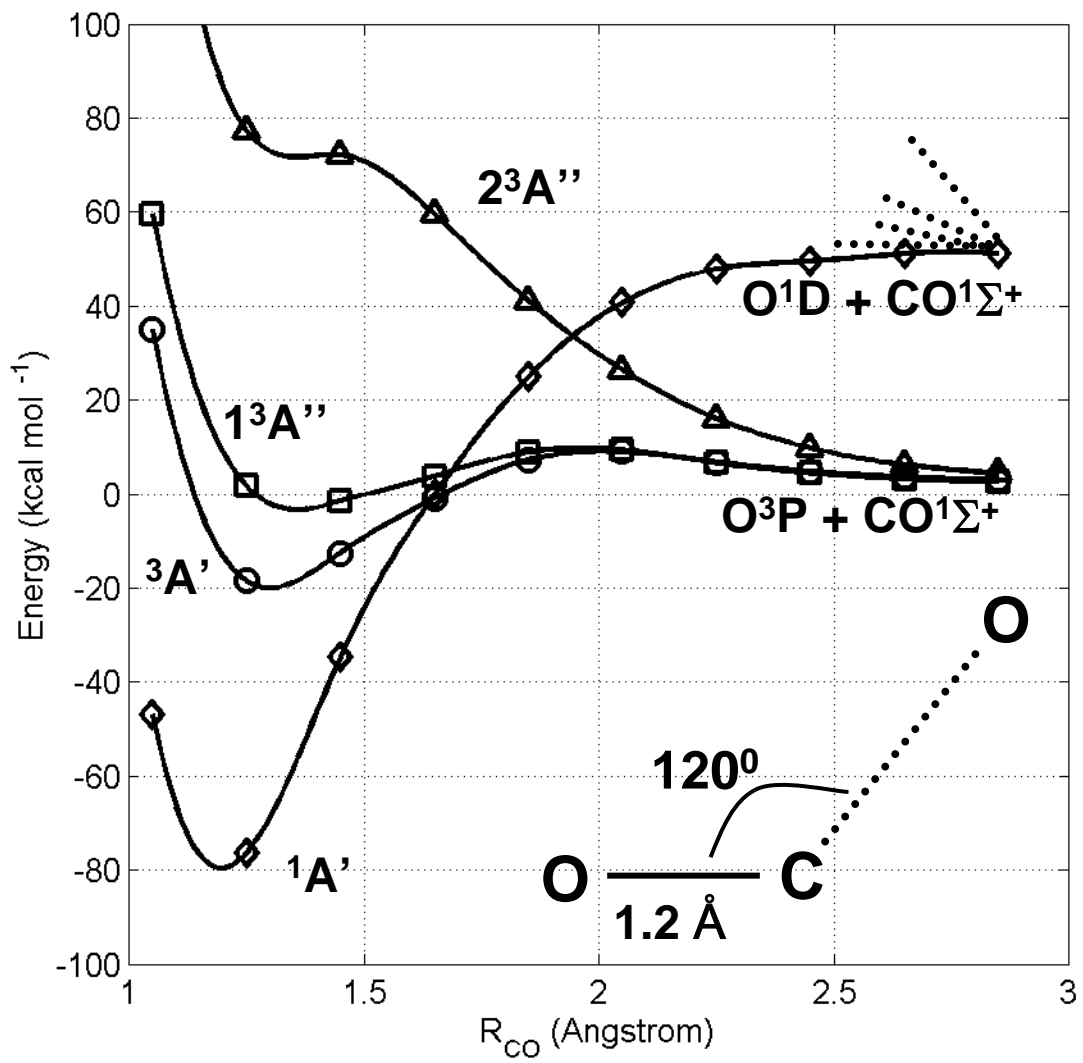


Figure 1

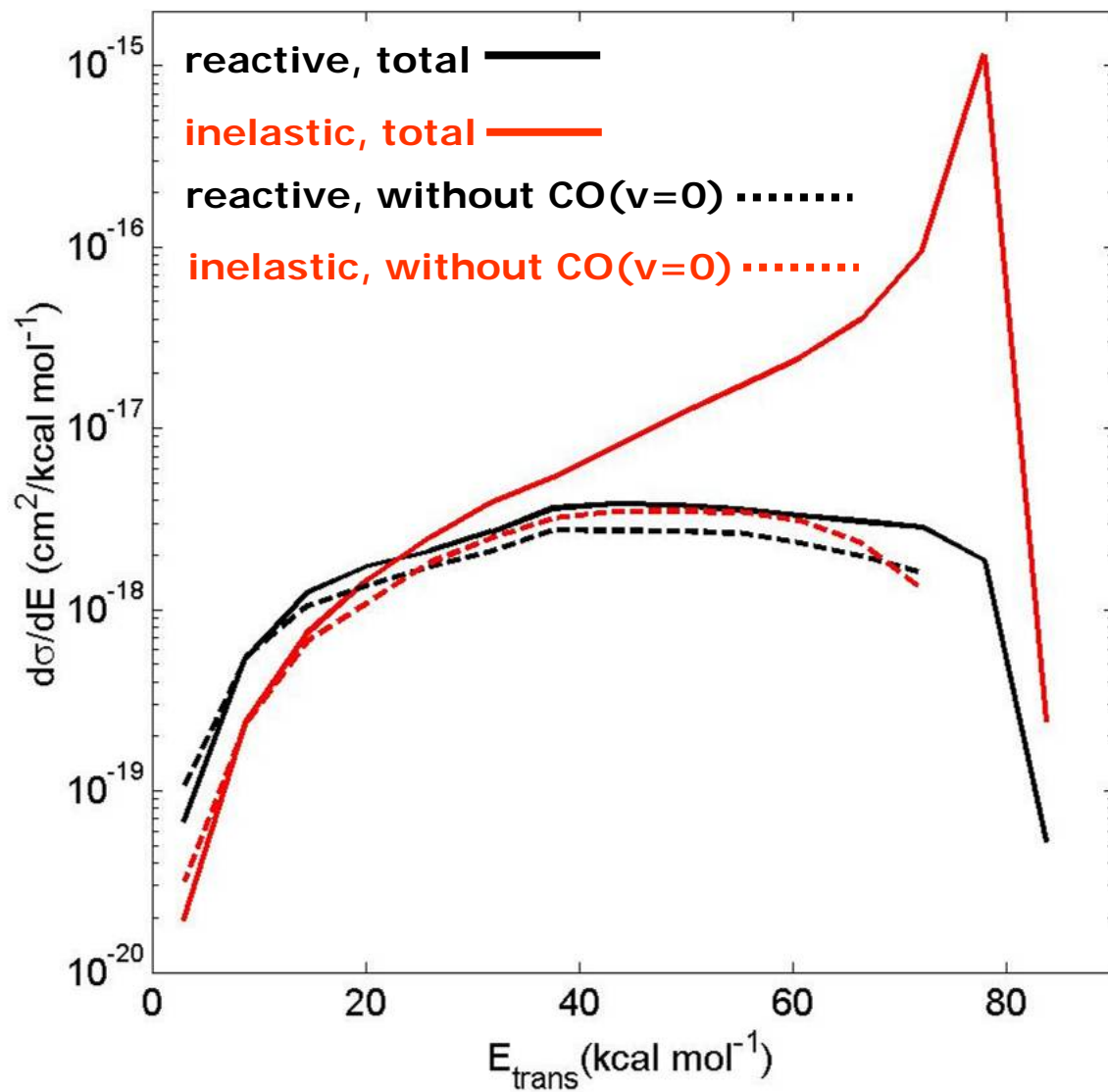


Figure 2

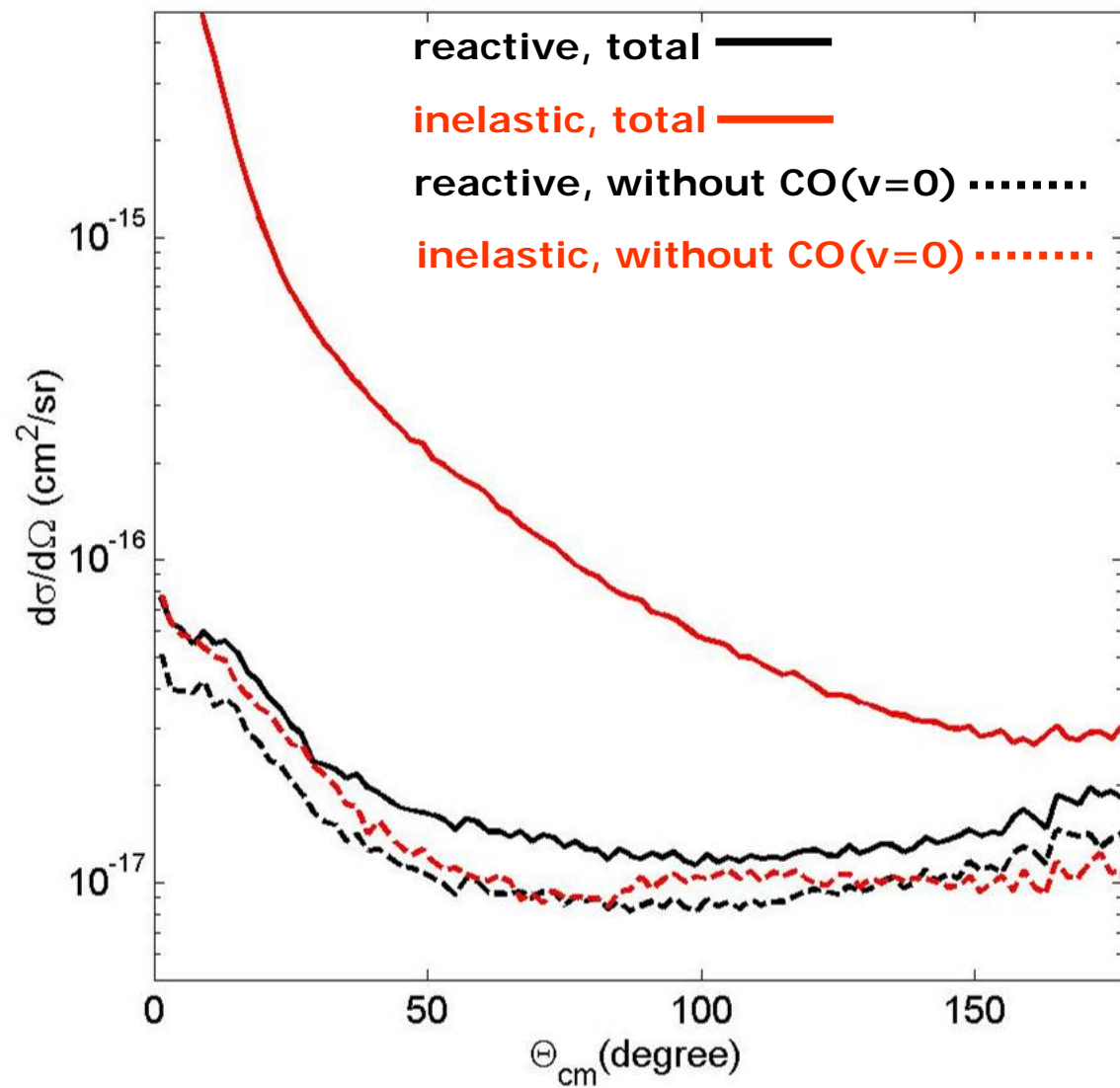


Figure 3

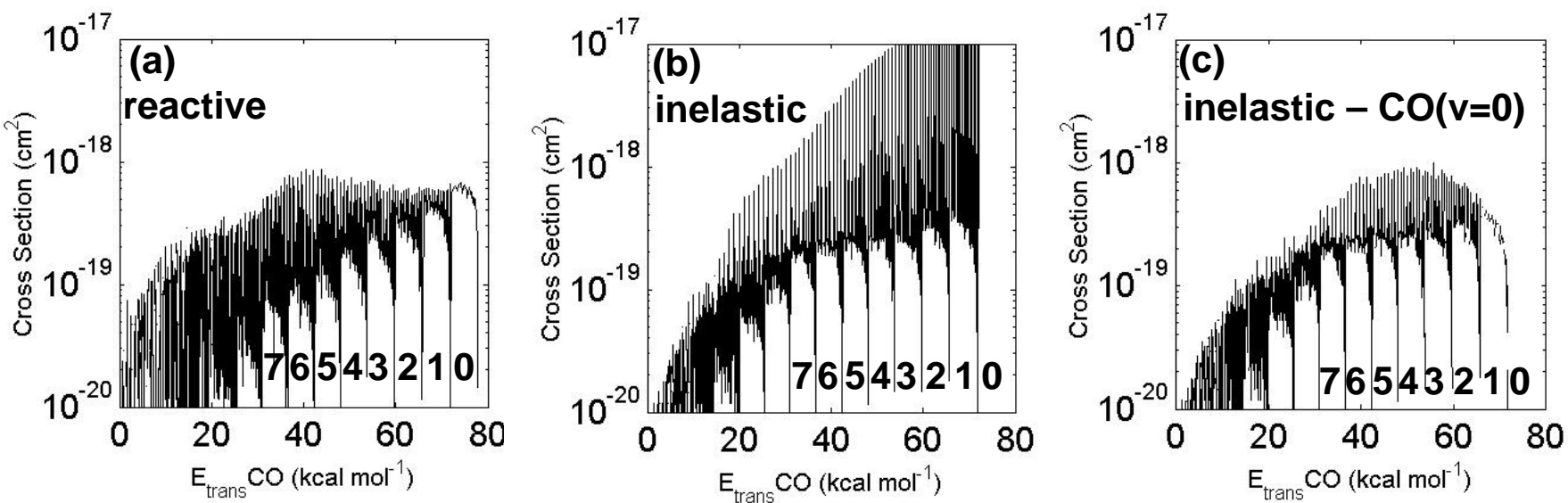


Figure 4

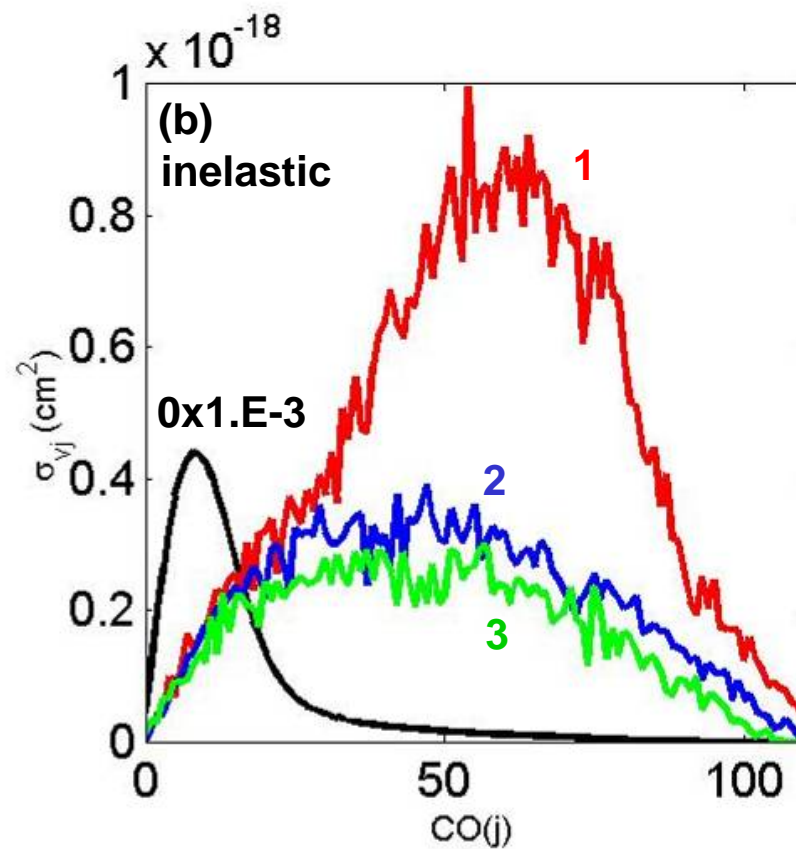
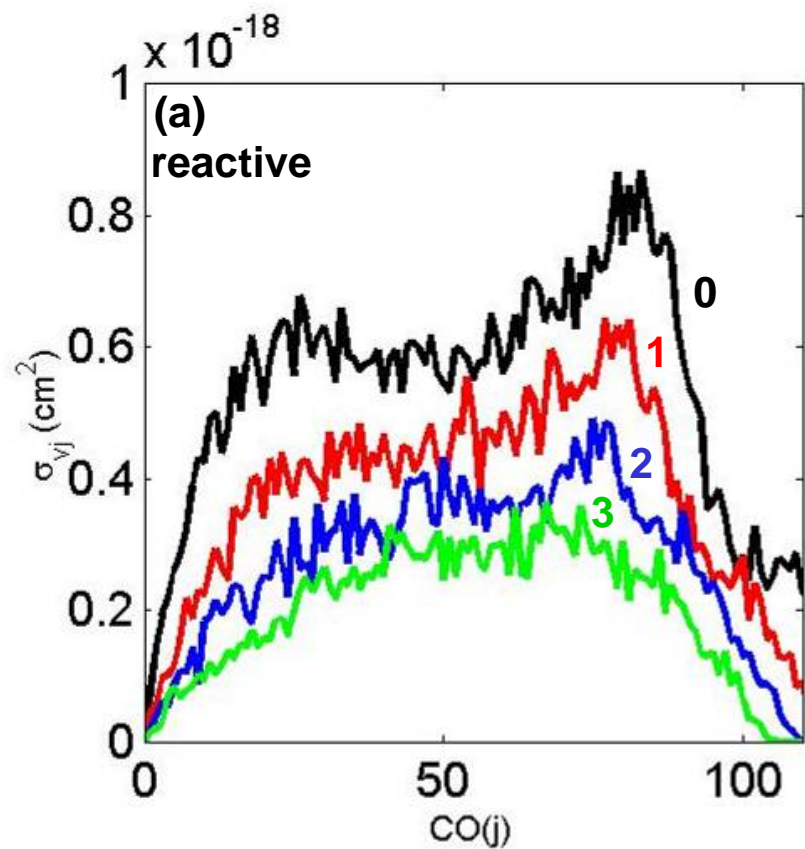


Figure 5

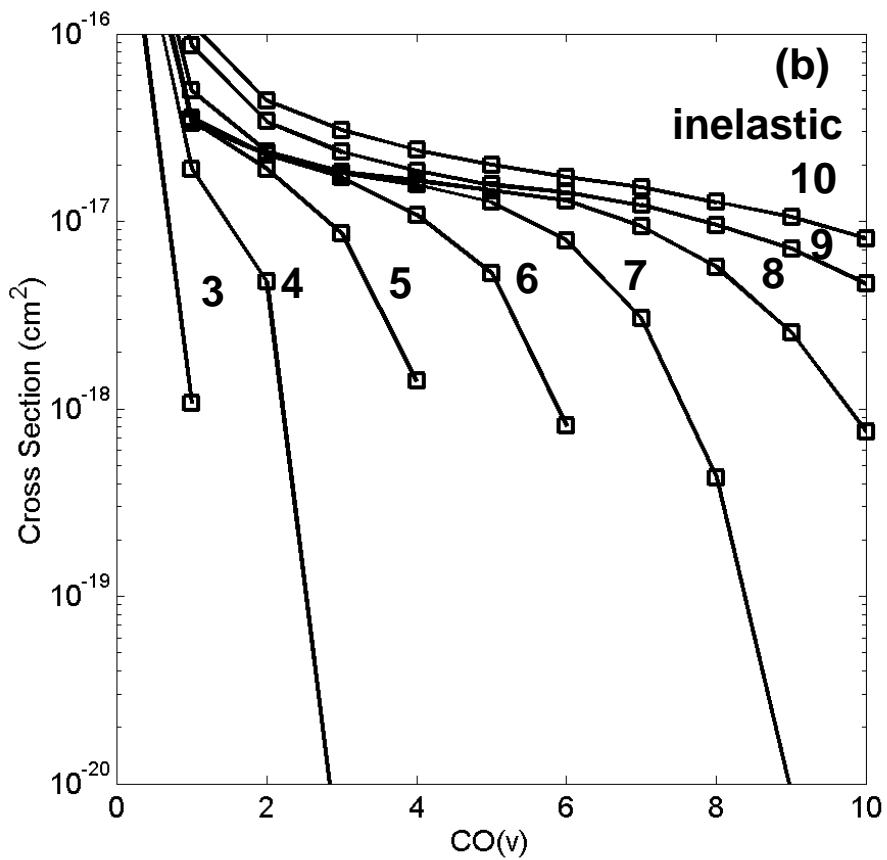
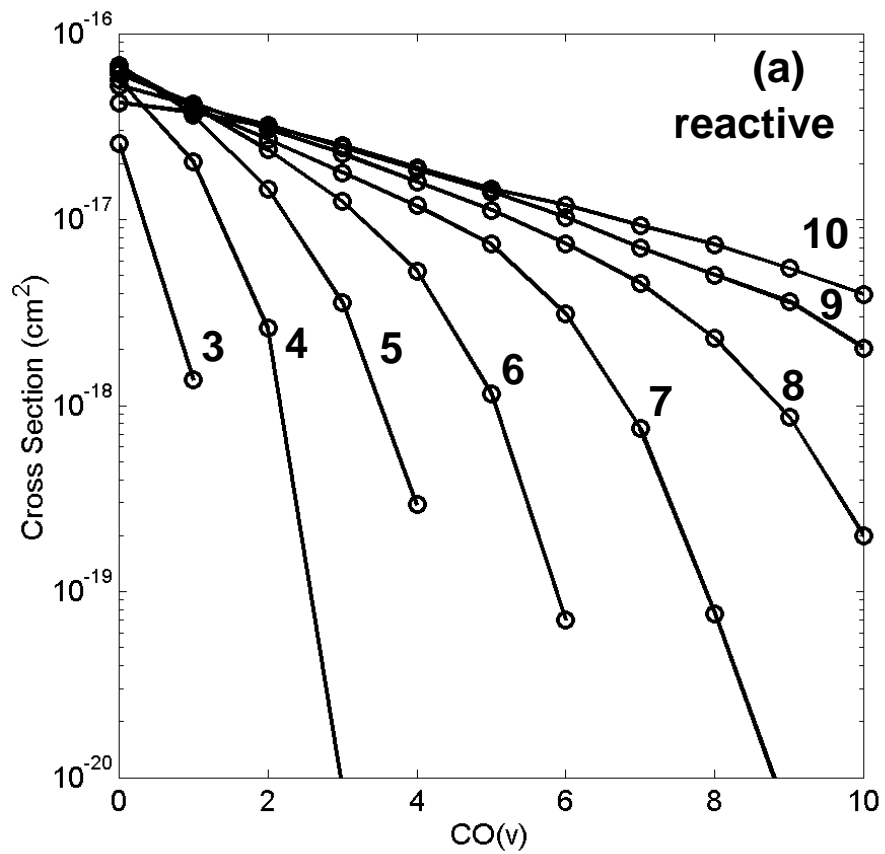


Figure 6

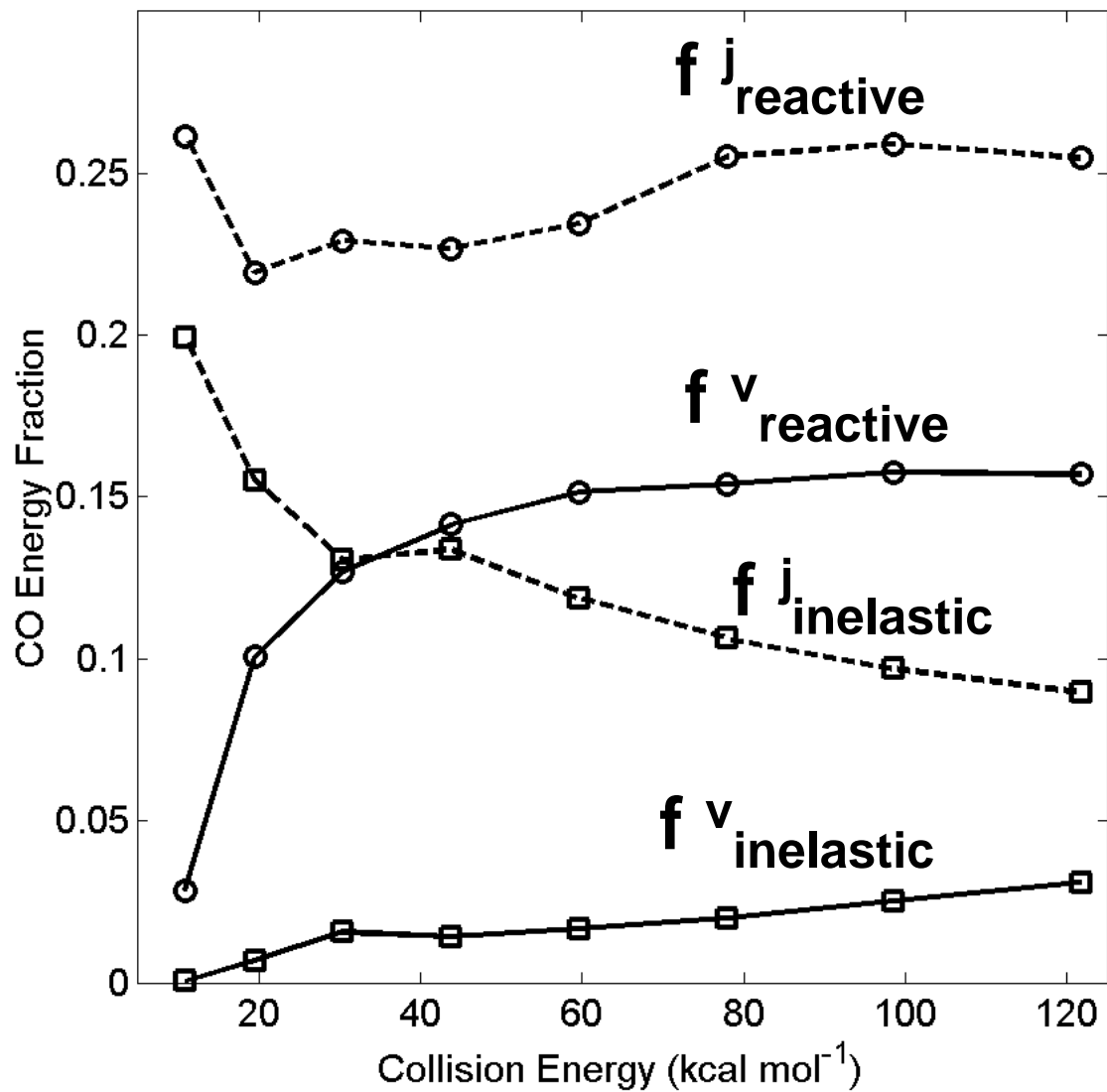


Figure 7

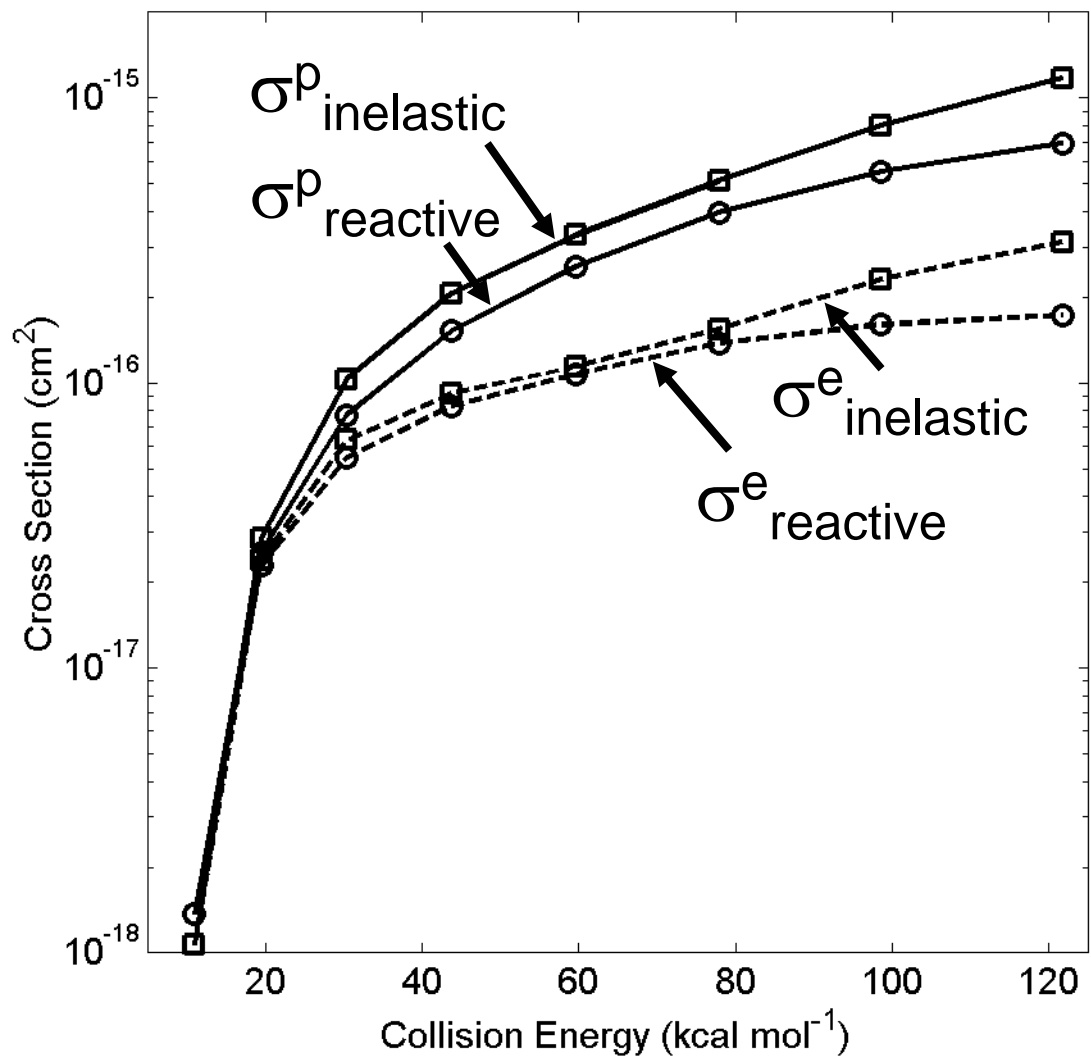
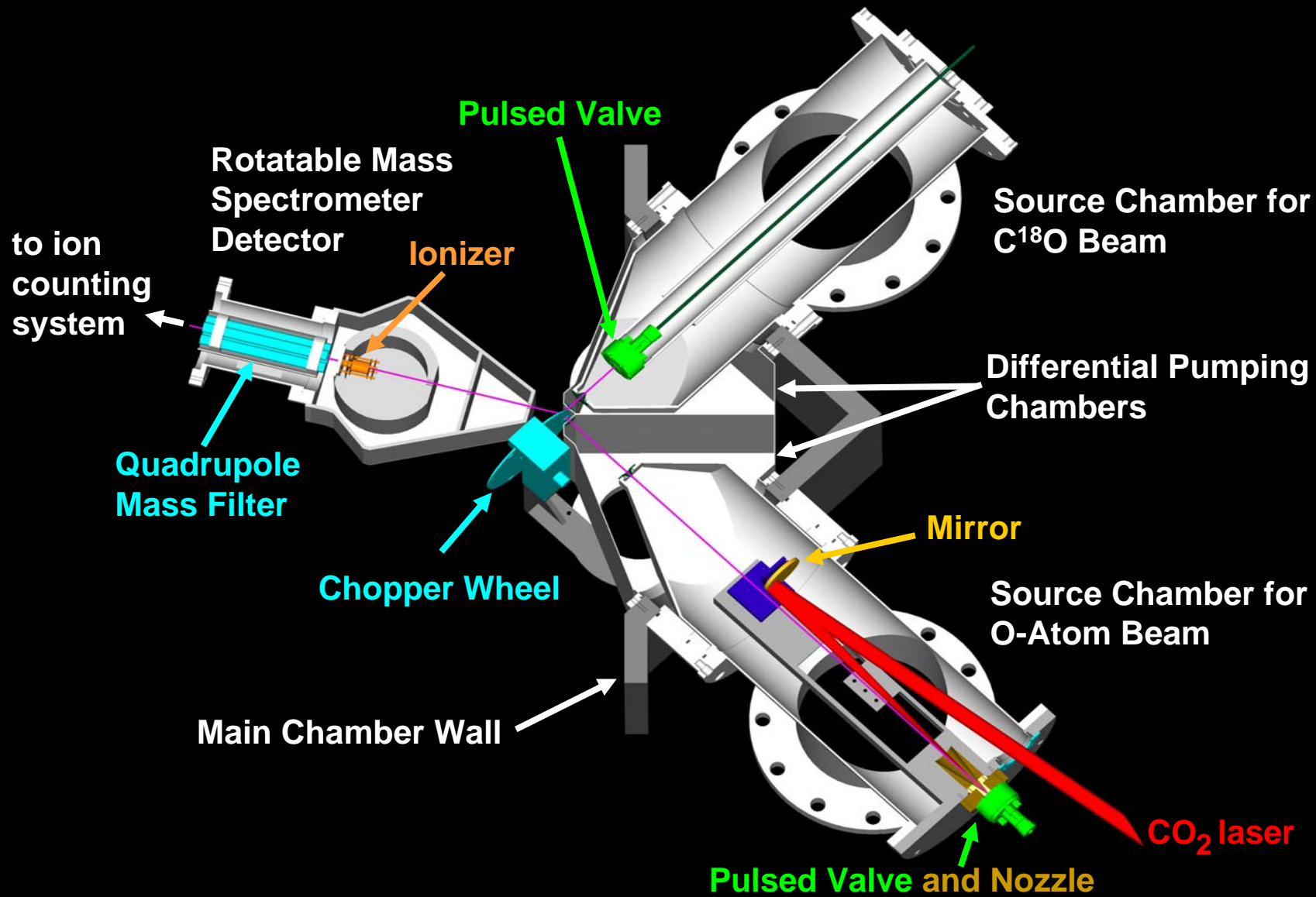


Figure 8



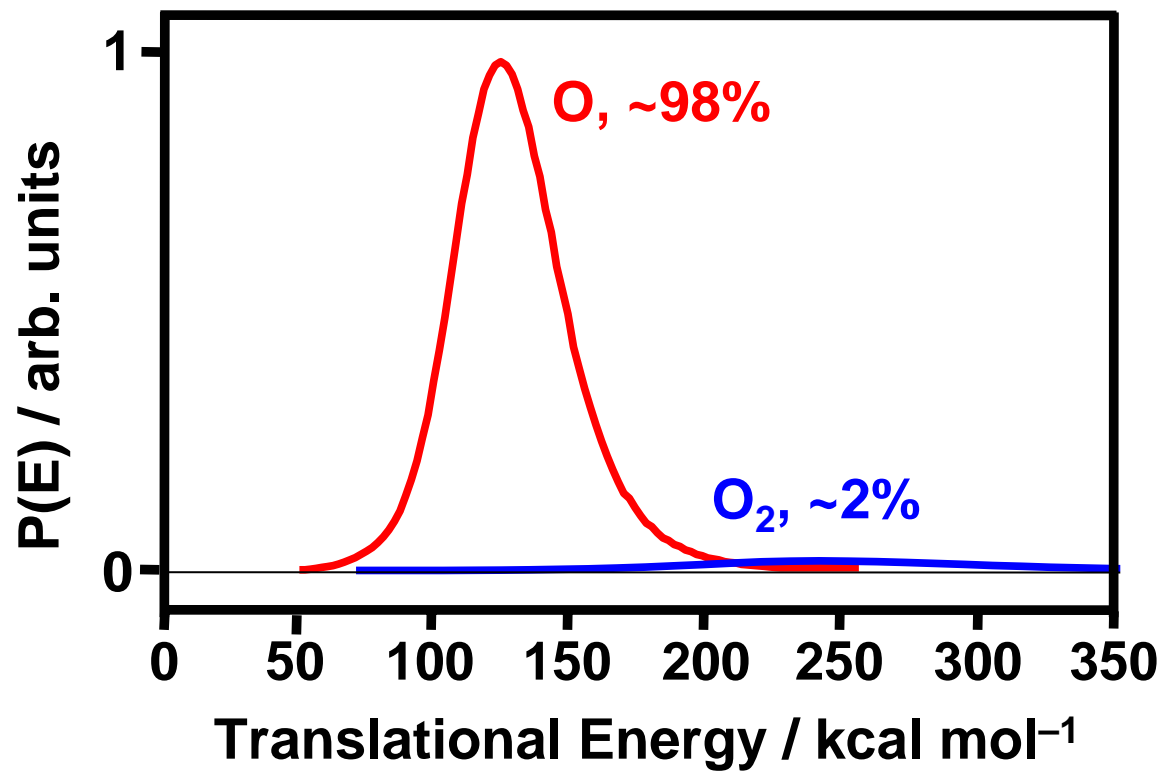


Figure 10

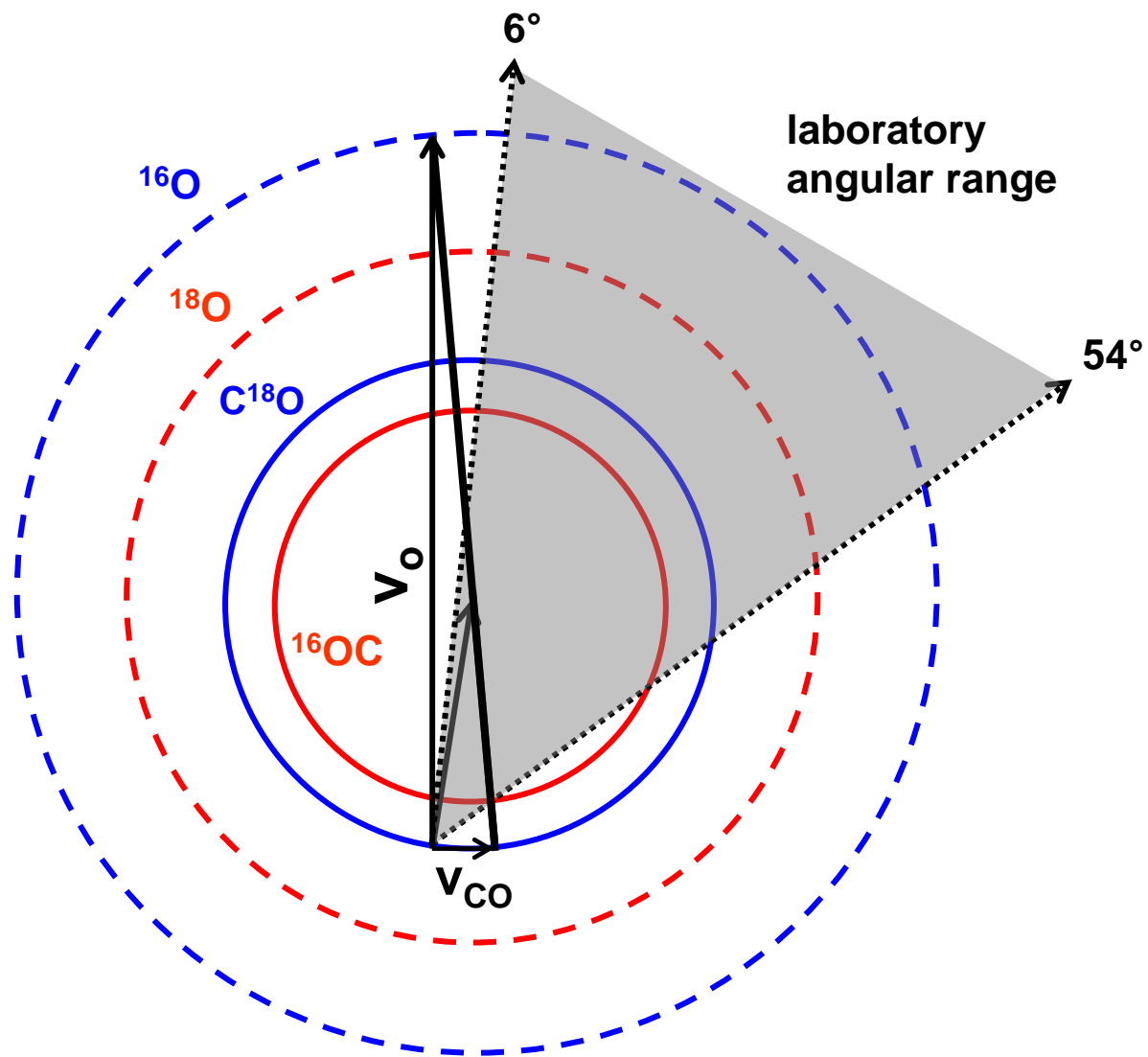


Figure 11

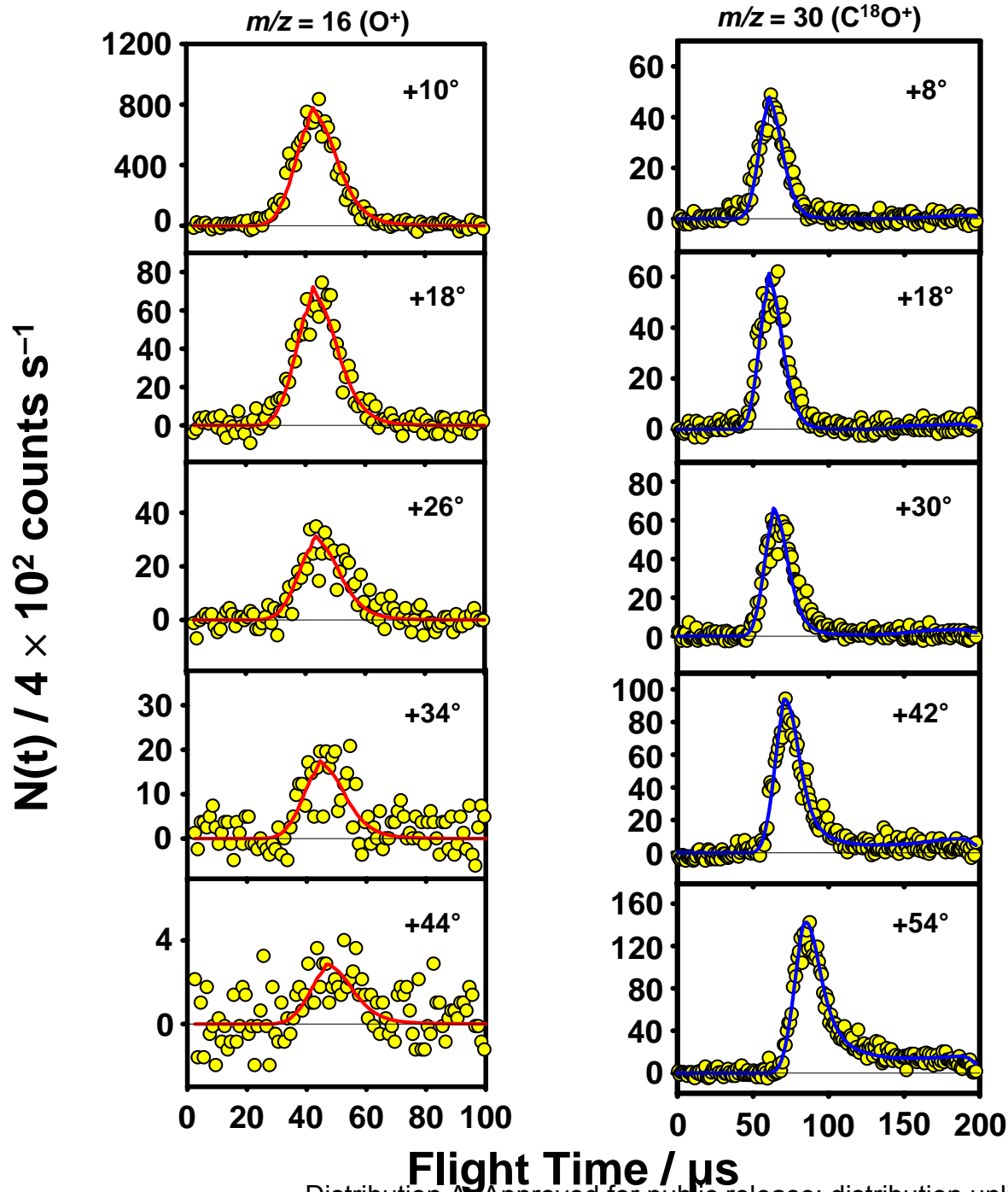


Figure 12

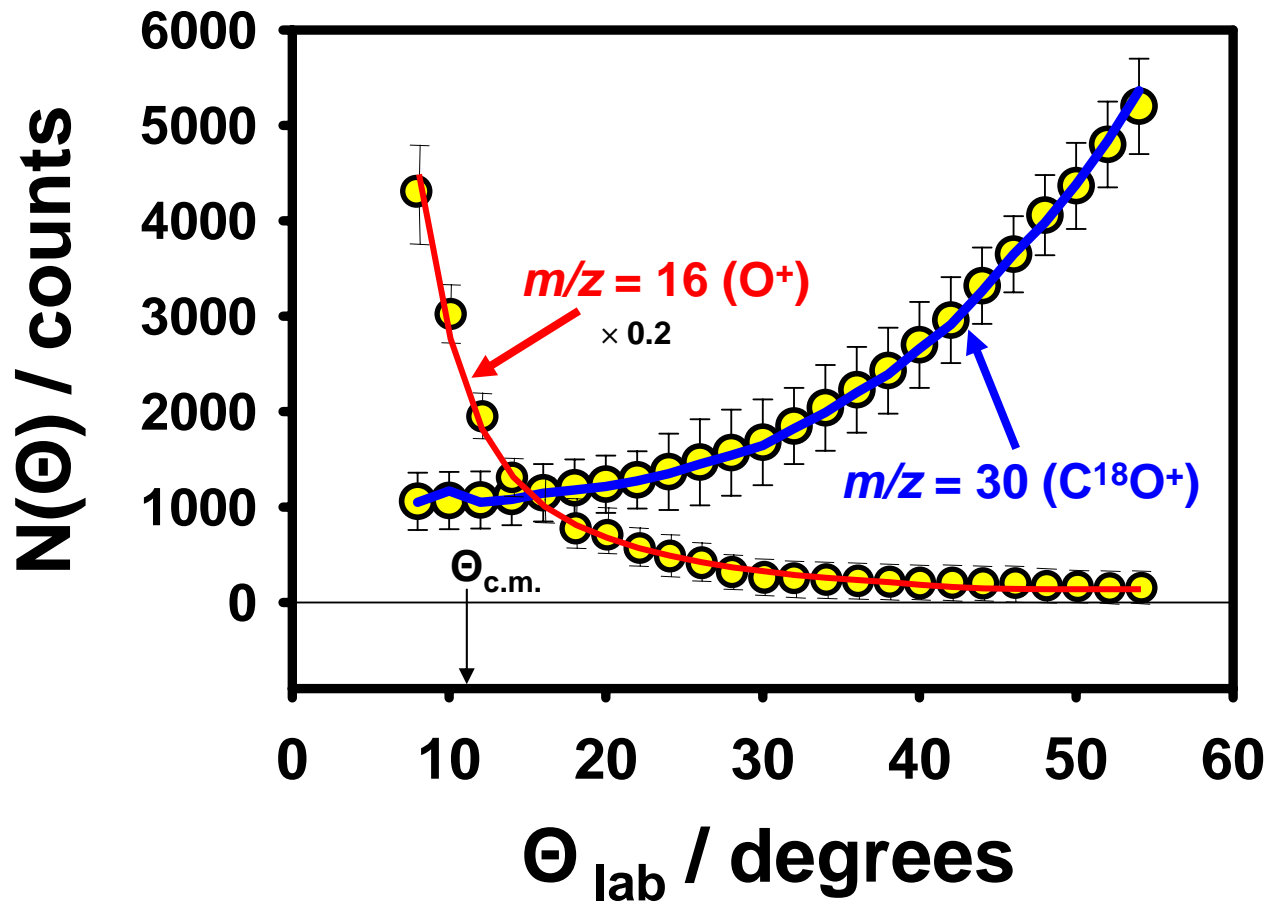


Figure 13

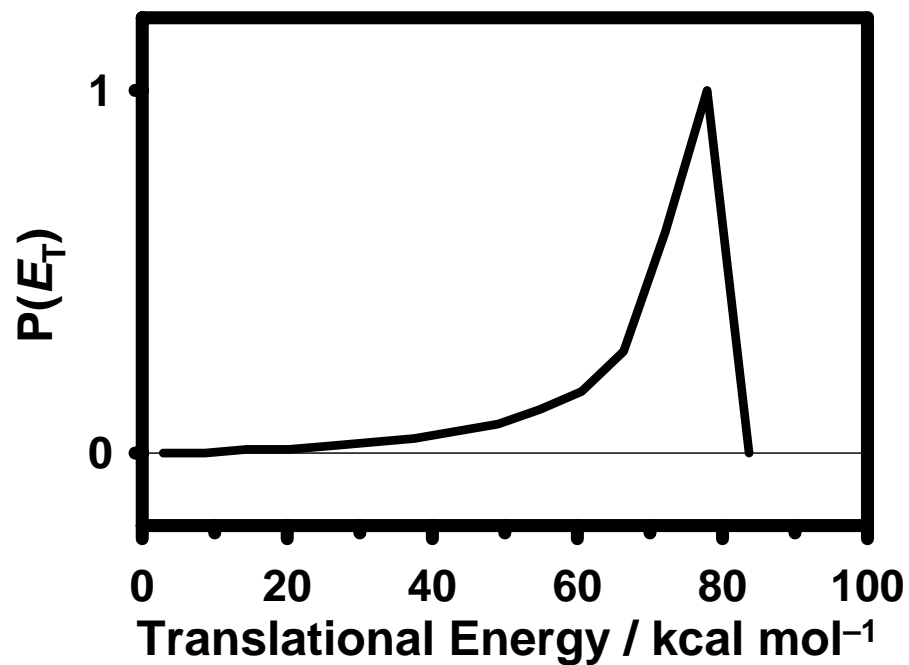
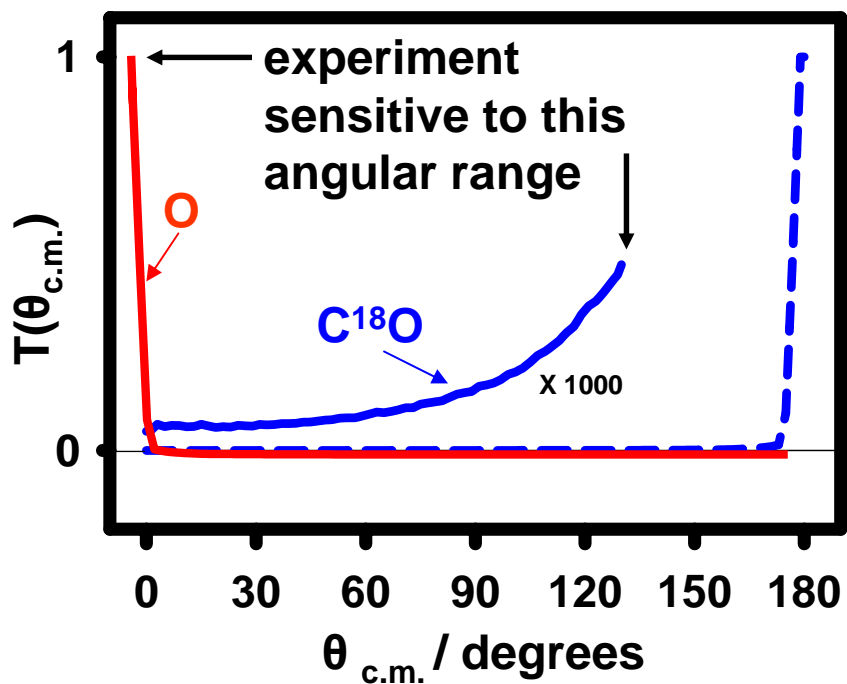


Figure 14

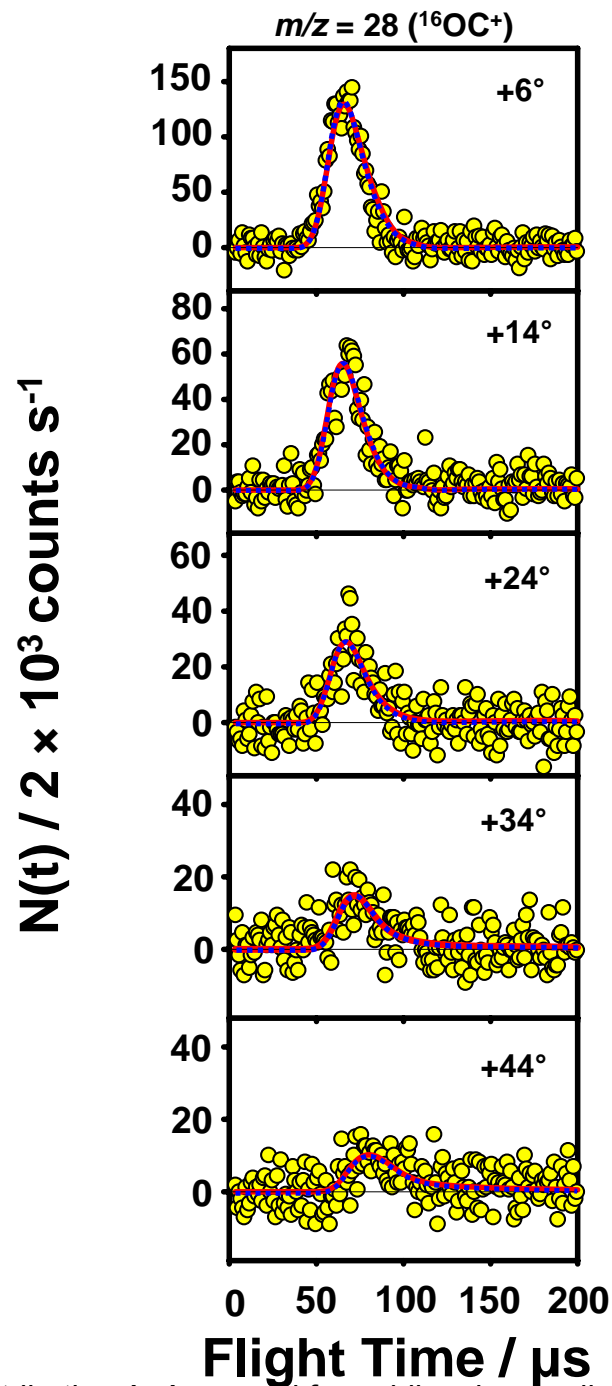


Figure 15

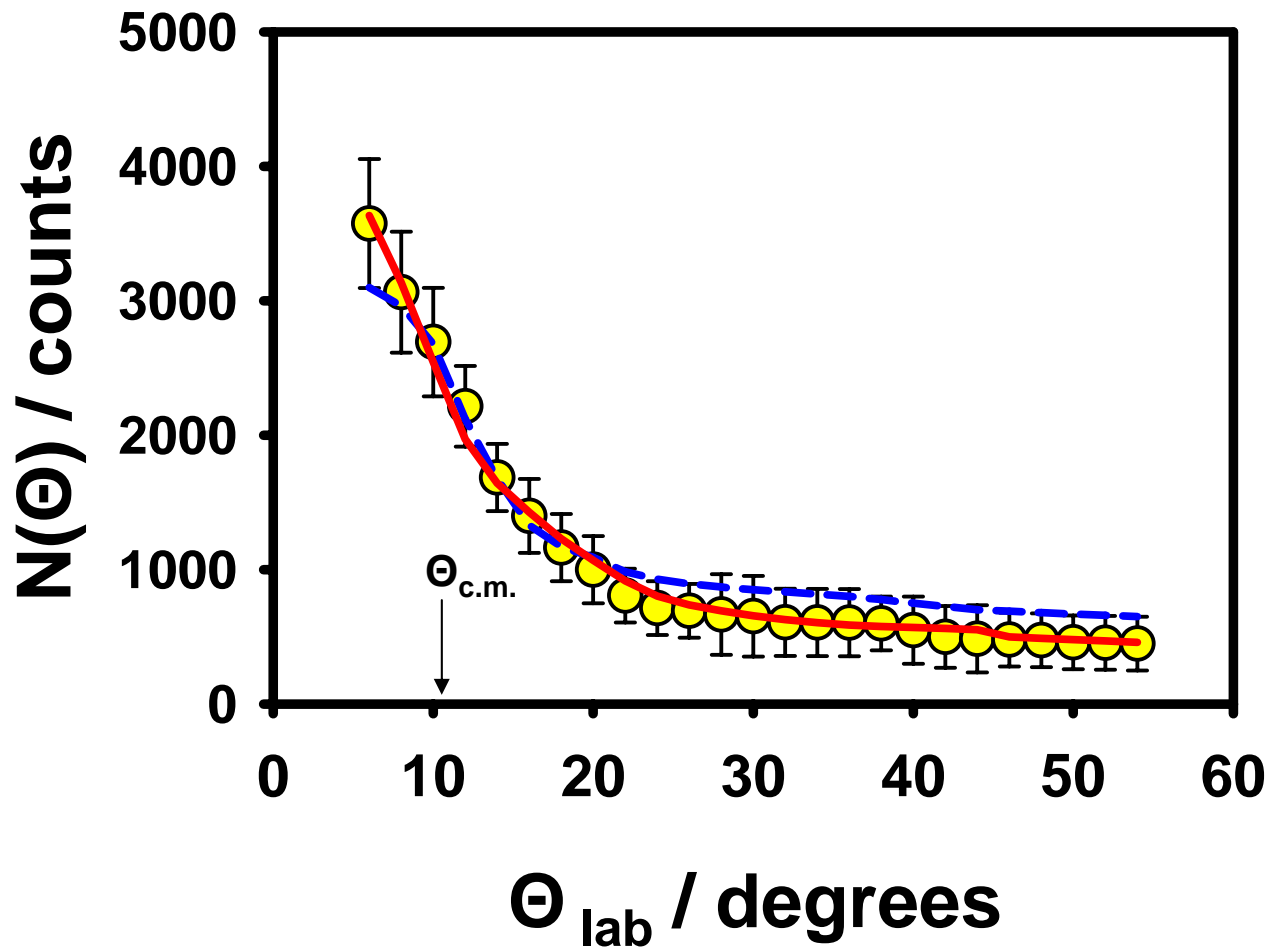


Figure 16

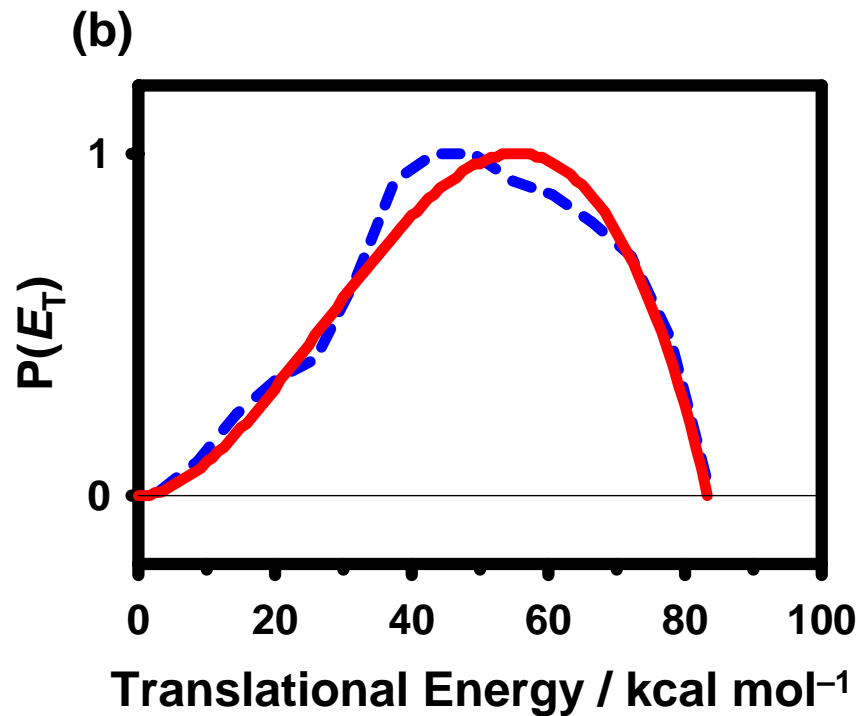
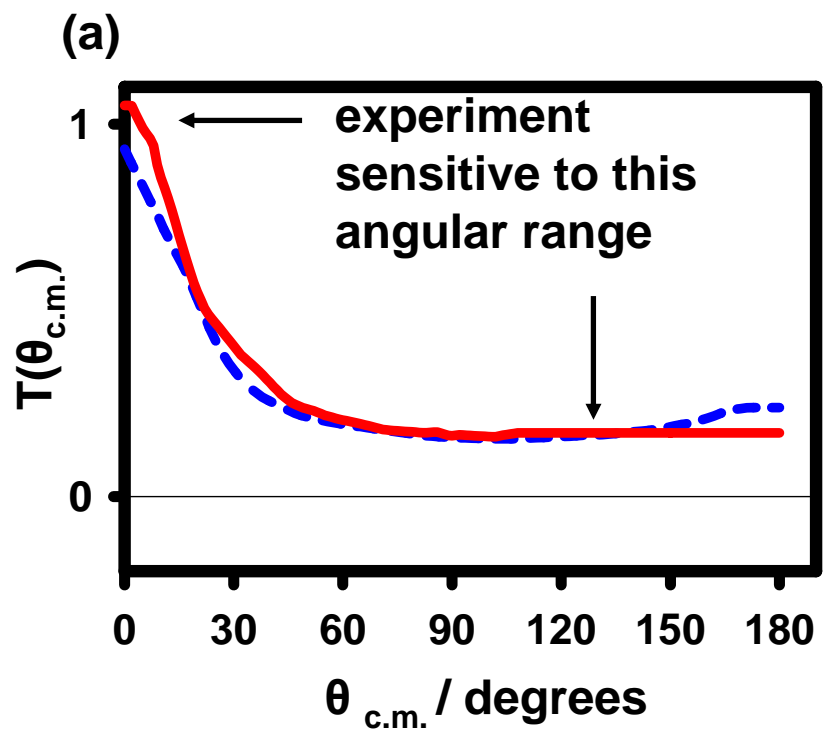
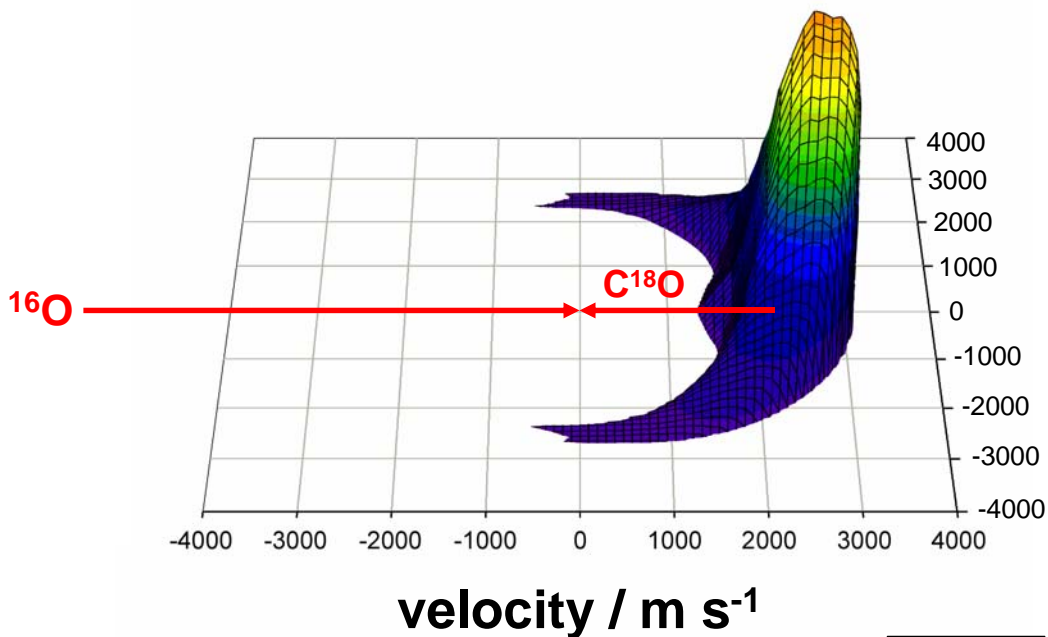


Figure 17

Experiment (a)



Theory (b)

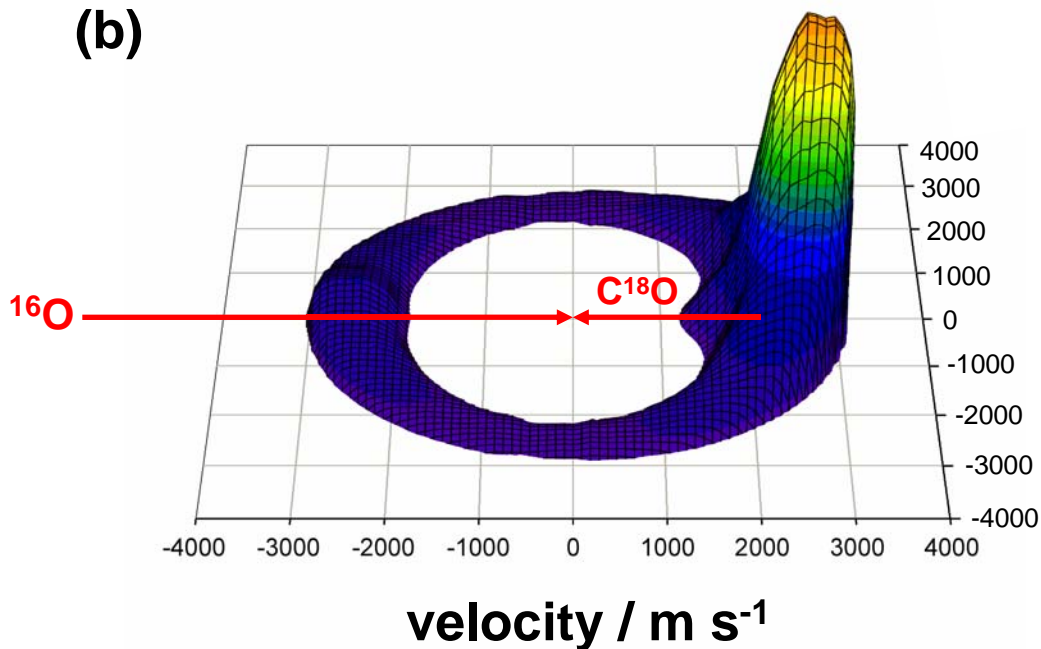


Figure 18

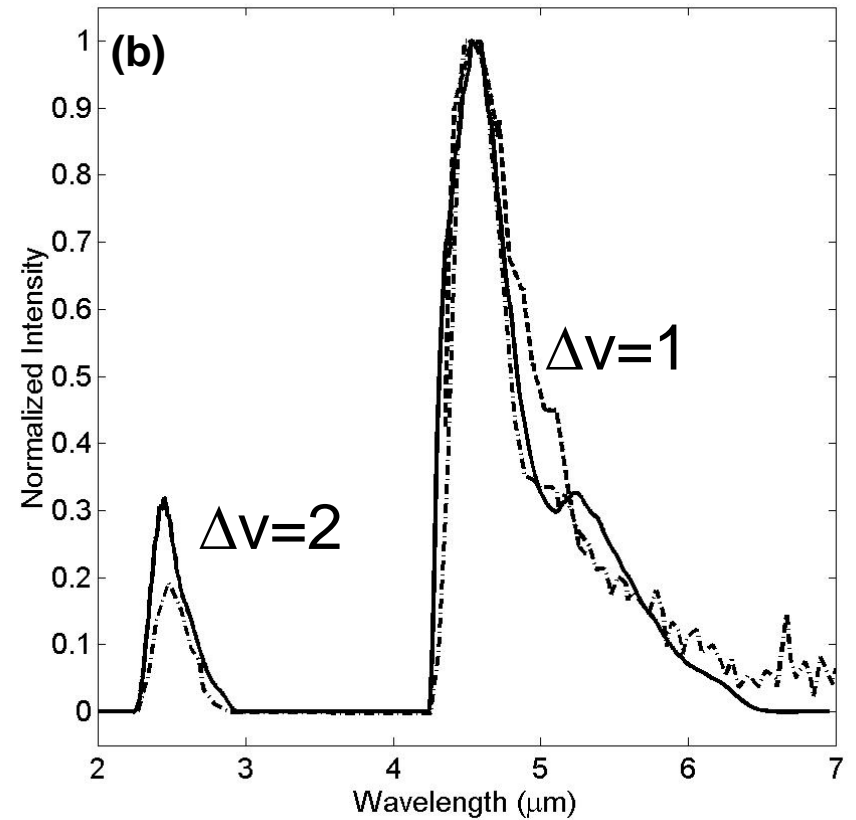
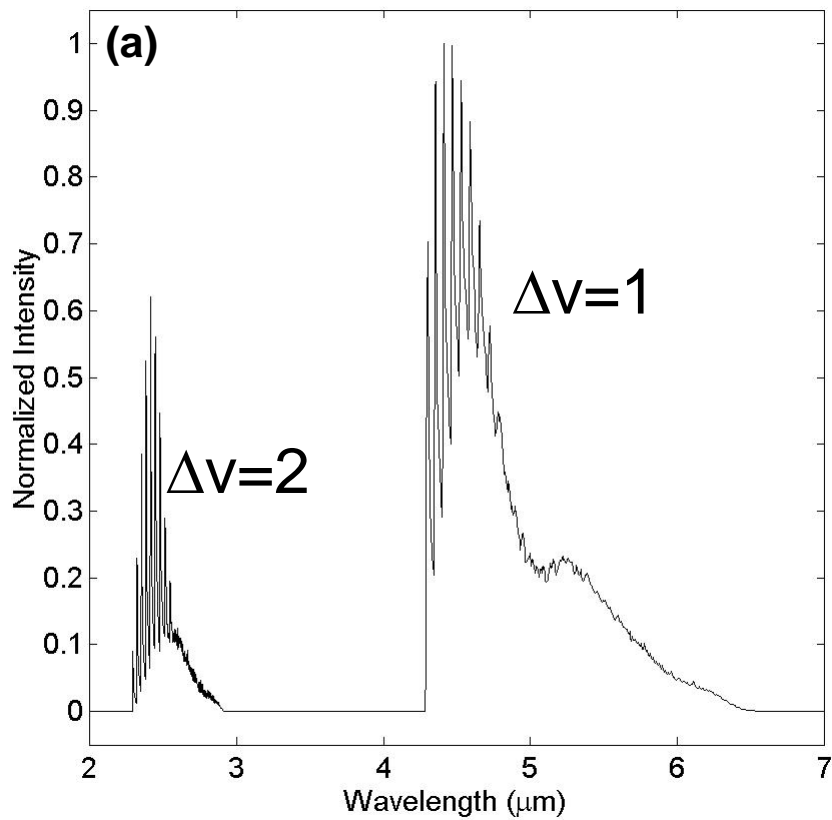


Figure 19

SUPPORTING INFORMATION

Representative animated trajectories of O + CO collisions are available as Supporting Information. These trajectories represent exchange of the oxygen atom that is bound to the carbon atom (reactive scattering) and collisional excitation of CO without exchange of the oxygen atom (inelastic scattering or “non-reactive” scattering). Some trajectories show the formation of a transient complex in which the three atoms linger together for a short time, usually less than a rotational period, before separating into products. This material will be available free of charge via the Internet as a Link associated with the manuscript.

General description:

O(3P) + CO collision trajectory movies at 8 km s⁻¹:

The molecular potential and methods are the same as M. Braunstein and J. Duff,

"Electronic Structure and Dynamics of O + CO Collisions", J. Chem. Phys., 112, 2736-2745 (2000).

The format is .avi. Each file contains ~10 trajectories and takes about two minutes of wall clock minutes to view. There are 30 files total in two folders for a total of ~560 Mbytes (uncompressed).

Detailed description and notation of movie plots:

O + CO Collision velocity 8 km s⁻¹

reactive_all folder -> all reactive collisions regardless of final CO(vibrational level

non_reactive_v_gt_0 folder -> non reactive (inelastic) collisions for CO(v>0) products

red sphere: incoming O-atom

black sphere: carbon atom

blue sphere: oxygen atom in target CO

O*(incoming) -> C--O(target)

red line O*C distance

green line C--O distance

blue line O*---O distance

b1-> 3A' state (lowest OCO triplet state)

a1-> 13A" state (second lowest OCO triplet state)

Each movie frame (sphere symbol) takes 4.8×10^{-15} seconds (4.8 fs = 200 au time).

Each trajectory is followed for approximately 1.25×10^{-13} seconds (125 fs)

The vibrational period of CO ranges from ~ 10 fs (CO(v=1)) to ~ 1 fs (CO(v=10))

The rotational period of CO ranges from $\sim 1. \times 10^4$ fs (CO(j=1)) to ~ 100 fs (CO(j=100))

All collisions occur at 8 km s^{-1} center of mass relative velocity (77.9 kcal mol⁻¹)

O(3P) + CO(v=0,j=300 K).

complex time => when $r_1 + r_2 + r_3$ (red line, green line, blue line) < 12 a.u.

fs = femtoseconds ($1. \times 10^{-15}$ seconds)

angle (center of mass scattering angle)

v# = final vibrational state

j# = final rotational state

etrans = final translational energy (kcal mol⁻¹)

Representative movie frames are shown below.

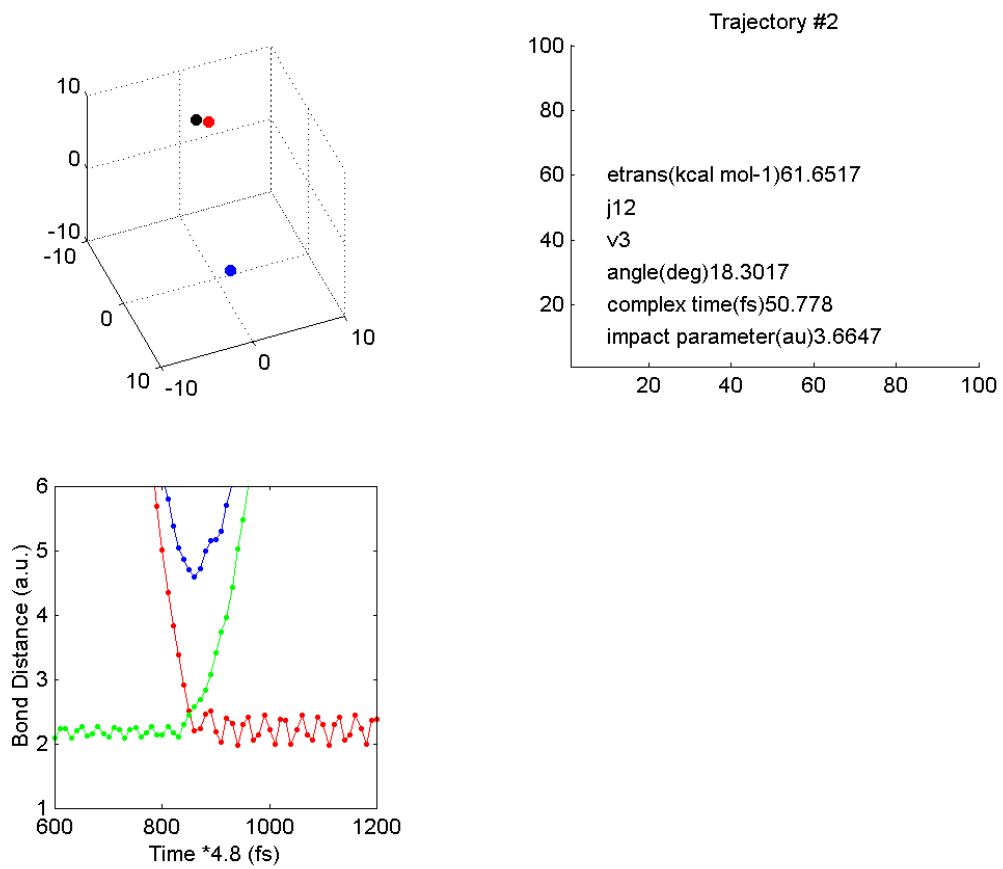


Figure 1. A1 Reactive trajectory

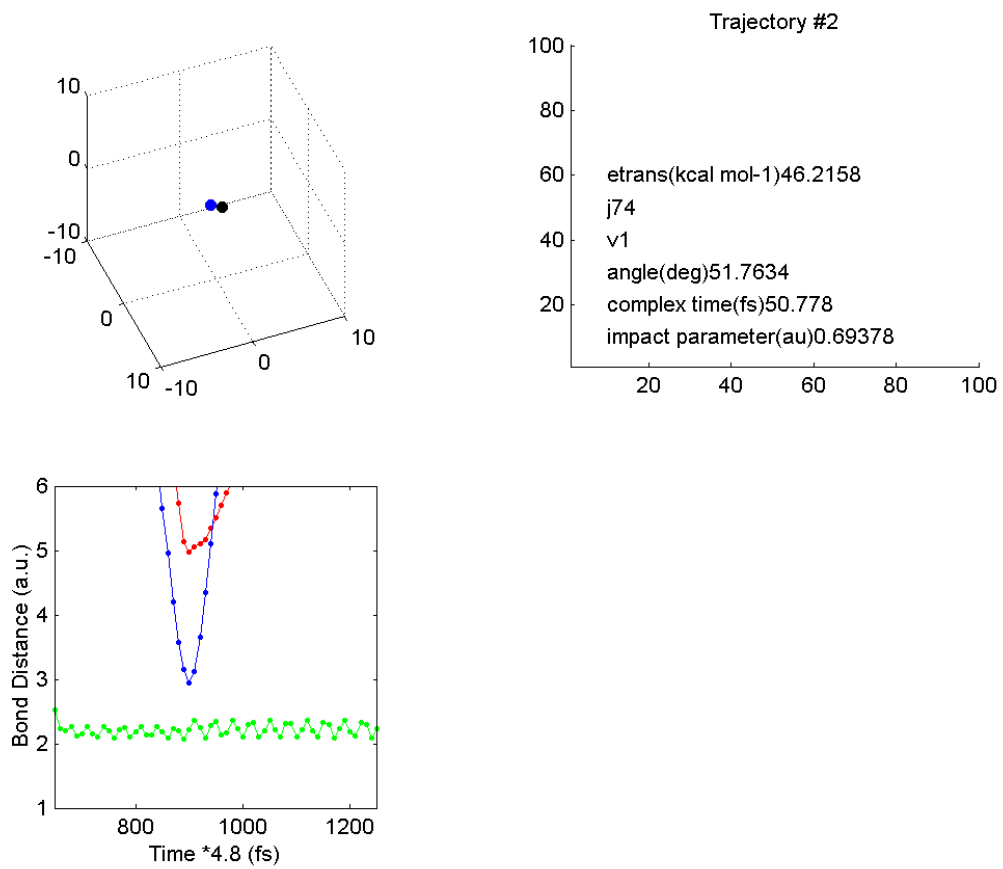


Figure 2. A1 Nonreactive (inelastic) trajectory

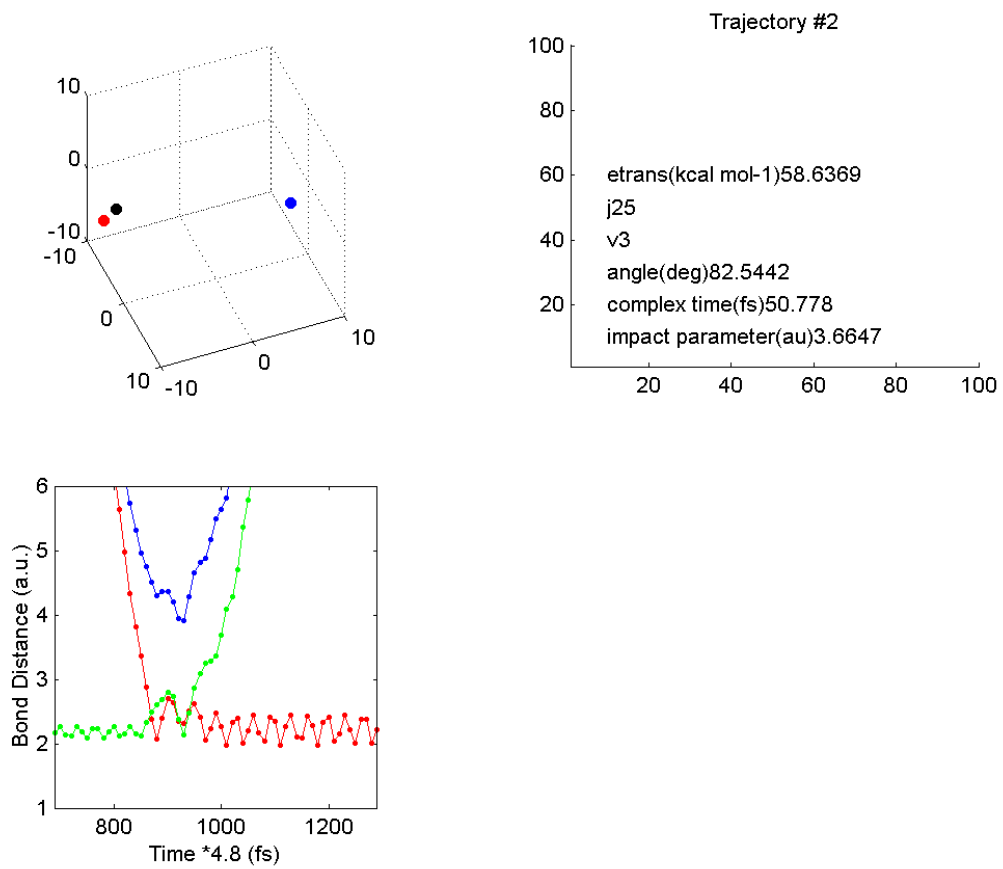


Figure 3. B1 Reactive trajectory

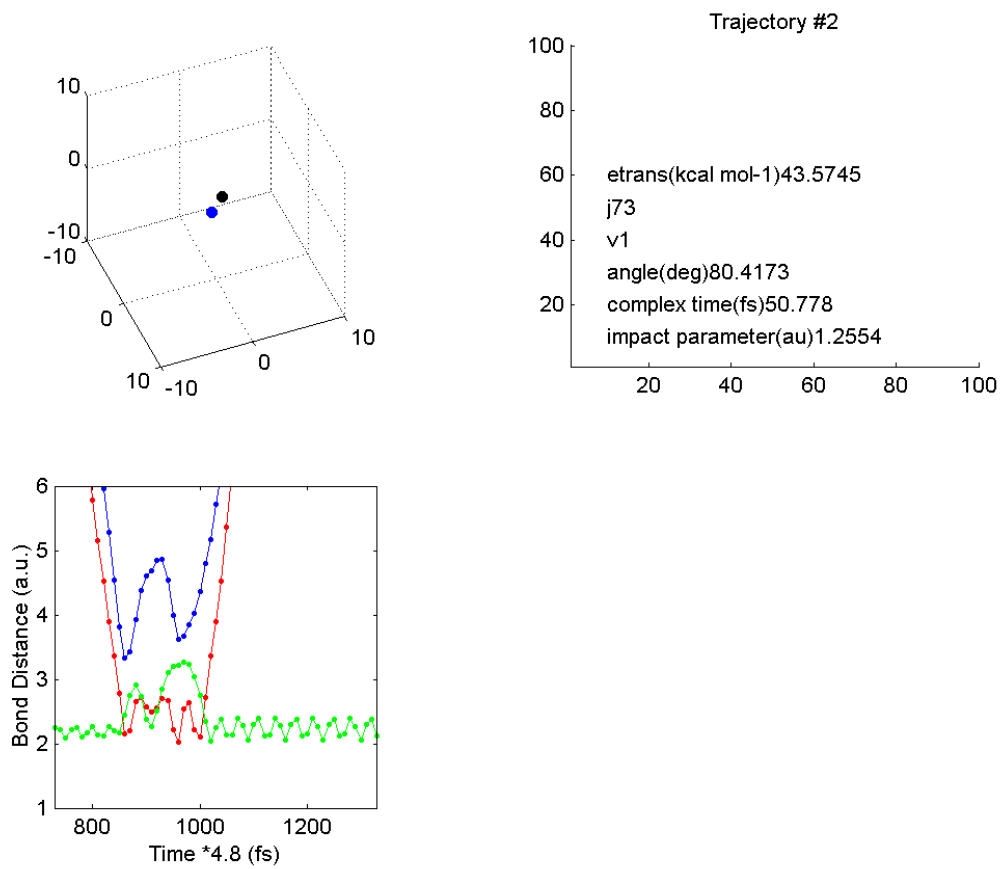


Figure 4. B1 Nonreactive (inelastic) trajectory